The Astrophysical Journal Supplement Series, 266:11 (20pp), 2023 May https://doi.org/10.3847/1538-4365/acc321

New Generation Stellar Spectral Libraries in the Optical and Near-infrared. I. The Recalibrated UVES-POP Library for Stellar Population Synthesis*

Sviatoslav B. Borisov[1], Igor V. Chilingarian[2,3], Evgenii V. Rubtsov[3,4], Cédric Ledoux[5], Claudio Melo[6], Kirill A. Grishin[7,3], Ivan Yu. Katkov[8,9,3], Vladimir S. Goradzhanov[3,4], Anton V. Afanasiev[10,3], Anastasia V. Kasparova[3], and Anna S. Saburova[3]

[1] Department of Astronomy, University of Geneva, Chemin Pegasi 51, 1290 Versoix, Switzerland; sviatoslav.borisov@unige.ch
[2] Center for Astrophysics—Harvard and Smithsonian, 60 Garden Street MS09, Cambridge, MA 02138, USA; igor.chilingarian@cfa.harvard.edu
[3] Sternberg Astronomical Institute, Moscow M.V. Lomonosov State University, 13 Universitetsky pr., Moscow 119234, Russia
[4] Faculty of Physics, Moscow M.V. Lomonosov State University, 1 Leninskie Gory, Moscow 119991, Russia
[5] European Southern Observatory, Alonso de Cordova 3107, Vitacura, Casilla 19001, Santiago de Chile, Chile
[6] Portuguese Space Agency, Estrada das Laranjeiras, No. 205, RC, 1649-018, Lisboa, Portugal
[7] Université de Paris-Cité, CNRS/IN2P3, Astroparticule et Cosmologie, F-75013 Paris, France
[8] New York University Abu Dhabi, Saadiyat Island, P.O. Box 129188, Abu Dhabi, UAE
[9] Center for Astro, Particle, and Planetary Physics, NYU Abu Dhabi, P.O. Box 129188, Abu Dhabi, UAE
[10] LESIA, Observatoire de Paris, Université PSL, CNRS, Sorbonne Université, Université Paris Cité, 5 place Jules Janssen, F-92195, Meudon, France
Received 2022 November 15; revised 2023 March 4; accepted 2023 March 6; published 2023 May 3

Abstract

We present reprocessed flux-calibrated spectra of 406 stars from the UVES-POP stellar library in the wavelength range 320–1025 nm, which can be used for stellar population synthesis. The spectra are provided in the two versions having spectral resolving power $R = 20{,}000$ and $R = 80{,}000$. Raw spectra from the ESO data archive were re-reduced using the latest version of the UVES data reduction pipeline with some additional algorithms that we developed. The most significant improvements in comparison with the original UVES-POP release are (i) an updated echelle order merging, which eliminates "ripples" present in the published spectra; (ii) a full telluric correction; (iii) merging of nonoverlapping UVES spectral setups taking into account the global continuum shape; (iv) a spectrophotometric correction and absolute flux calibration; and (v) estimates of the interstellar extinction. For 364 stars from our sample, we computed atmospheric parameters $T_{\rm eff}$, surface gravity $\log g$, metallicity [Fe/H], and α-element enhancement [α/Fe] by using a full-spectrum fitting technique based on a grid of synthetic stellar atmospheres and a novel minimization algorithm. We also provide projected rotational velocity $v \sin i$ and radial velocity $v_{\rm rad}$ estimates. The overall absolute flux uncertainty in the reprocessed data set is better than 2%, with subpercent accuracy for about half of the stars. A comparison of the recalibrated UVES-POP spectra with other spectral libraries shows a very good agreement in flux; at the same time, Gaia DR3 BP/RP spectra are often discrepant with our data, which we attribute to spectrophotometric calibration issues in Gaia DR3.

Unified Astronomy Thesaurus concepts: Stellar atmospheres (1584); Stellar abundances (1577); Stellar effective temperatures (1597); Stellar populations (1622); Astronomy databases (83); Star atlases (1566); Astronomical reference materials (90)

Supporting material: machine-readable table

1. Introduction

High-quality models of stellar populations play a crucial role in modern astrophysics—they are used for interpreting galaxy and star cluster data to determine the age, metallicity, chemical abundances, and other properties (e.g., Guiderdoni & Rocca-Volmerange 1987; Bruzual & Charlot 2003; González Delgado et al. 2005; Vazdekis et al. 2010). For the vast majority of stellar systems, only integrated light characteristics are available, such as colors and/or spectra integrated along the line of sight, which is a sum of contributions from individual stars that are too faint and/or too crowded to be observed single-handedly. Spectra of synthetic stellar populations are used to interpret such data sets and infer star formation and chemical enrichment histories of galaxies and their subsystems. An essential ingredient of stellar population synthesis is a library of stellar spectra, which is a set of spectra of stars in some particular wavelength range and having the same spectral resolution. Stars composing a spectral library should have the widest possible coverage in physical parameters of stellar atmospheres, such as the effective temperature $T_{\rm eff}$, surface gravity $\log g$, iron abundance [Fe/H], and α-element enhancement [α/Fe] (and sometimes abundances of individual chemical elements, micro- and macroturbulent velocities, etc.). Table 1 represents the list of some empirical stellar spectral libraries and their characteristics.

In this paper, we describe the recalibration process of the UVES-POP stellar spectral library (UVES Paranal Observatory Project; Bagnulo et al. 2003), which includes spectra of 406 stars observed with the Ultraviolet and Visual Echelle Spectrograph (UVES; Dekker et al. 2000) operated at ESO VLT UT2. The motivation for our project was that most empirical fully calibrated stellar spectra have either high resolution but rather short wavelength range or wide spectral

* Recalibrated spectra are available at https://sl.voxastro.org/.

Table 1
Characteristics of Several Widely Used Stellar Libraries

Library	Resolving Power R	Wavelength Range (nm)	Number of Stars	Reference
UVES-POP	80,000	304–1040	359	Bagnulo et al. (2003)
SpecMatch-Emp	60,000[a]	499–641	404	Yee et al. (2017)
ELODIE	10,000	390–680	1388	Prugniel & Soubiran (2001),
	42,000[a]	390–680	1388	Prugniel et al. (2007)
X-Shooter	10,000	300–1020	237	Chen et al. (2014),
	10,000	300–2450	666	Gonneau et al. (2020) (DR2),
	10,000	350–2480	683	Verro et al. (2022) (DR3)
Indo-US	5000	346–946	1273	Valdes et al. (2004)
MILES	2000	352–750	985	Sánchez-Blázquez et al. (2006)
STELIB	2000	320–930	249	Le Borgne et al. (2003)
IRTF	2000	800–5000	210	Rayner et al. (2009)
	2000	700–2500	284	Villaume et al. (2017)
MaStar	1800	362–1035	3321	Yan et al. (2019)
LW2000	1100	500–2500	100	Lançon & Wood (2000)
NGSL	1000	168–1020	378	Gregg et al. (2006)

Note. The information about UVES-POP refers to the original release.
[a] Continuum normalized spectra.

coverage but low to intermediate resolution. The resolving power of the UVES-POP spectra is $R \sim 80{,}000$ while covering the wavelength range from 304 to 1040 nm almost contiguously. The main goals of the UVES-POP library recalibration project are to improve the merging of echelle orders and to perform telluric correction, spectrophotometric calibration, and correction for interstellar extinction, so as to make spectra usable for stellar population synthesis. In addition, we present atmospheric parameters of UVES-POP stars computed with a novel full-spectrum fitting technique.

2. The Original UVES-POP Stellar Library: The Sample

The original UVES-POP stellar spectral library contains spectra of around 400 stars with a resolving power of $R = 80{,}000$. The stars were observed with UVES using a $0\farcs5$-wide slit in two instrument modes, combining Dichroic #1 and Dichroic #2, in order to cover the wavelength range from 300 to 1040 nm contiguously with only a few narrow gaps. Observations were carried out between 2001 February and 2003 March under ESO program 266.D-5655(A). We selected all stars from the UVES ESO archive for that program and downloaded the original unprocessed data. We also downloaded calibration frames collected as close as possible in time to the science frames. In our sample, there are several targets that were not included in the final sample of the original UVES-POP library because they did not pass quality control. In total, the new recalibrated UVES-POP library contains spectra of 406 stars, 262 of which have spectra covering the full optical wavelength range. Figure 1 presents the distribution of stellar types of the targets that we used in our project.

The UVES-POP library includes two groups of stars: field stars and stars in open clusters. The former were selected to cover the largest possible variety of stellar types across the Hertzsprung–Russell diagram. Stars from the second group belong to the two young open clusters IC 2391 (age $\approx$ 40 Myr; Barrado y Navascués et al. 2004) and NGC 6475 (age $\approx$ 200 Myr; Villanova et al. 2009), so that the stars in each cluster should have similar chemical abundances.

3. Data Reduction and Calibration

3.1. Preliminary Reduction with the UVES Pipeline

We used the UVES pipeline (Ballester et al. 2000) through EsoRex (ESO Recipe Execution Tool; ESO CPL Development Team 2015) to process the raw 2D UVES data, which include science and calibration frames (bias, format check file, order definition flat, echelle flat, dark, and a spectrum of the ThAr wavelength calibration lamp). All of them were taken on the same night as the corresponding science frames, except for the dark frames, which were taken 3 times per month for the purposes of detector monitoring. To run the full data reduction chain, we used the UVES_OBS_REDCHAIN recipe, which performs the following steps: (i) creation of a master bias frame, (ii) implementation of the UVES instrument model, (iii) tracing of echelle orders positions, (iv) construction of a master flat-field frame, (v) wavelength calibration, and (vi) reduction of the science frame. The pipeline performs an optimal extraction of the object spectrum and produces the following output files: six spectral segments of spectra with uncertainties (in both merged and resampled formats), and a resampled blaze function. All the output products are one-dimensional. The six segments correspond to different setups, which are produced by the combination of two different optical paths and three CCD detectors. Table 2 gives the list of UVES setups and associated wavelength ranges.

3.2. Calibration and Merging of Echelle Orders

A noticeable feature of the standard pipeline-reduced UVES-POP spectra is a set of ripples in the regions where echelle orders overlap. In some spectra from the original stellar library, these ripples substantially deteriorate the final product quality. This occurs for two main reasons. First, the pupil illumination is slightly different between calibrations and science frames. This results in a different blaze definition and in particular a shift between, e.g., science frames and the internal flat fields (Bowers & Lindler 2003), which are used to correct for the blaze function. Nonideal centering of the field derotator, for instance, could cause tiny pupil offsets. In addition, UVES is not fully sealed, so small temperature and/or pressure variations inside the instrument can induce an offset in the

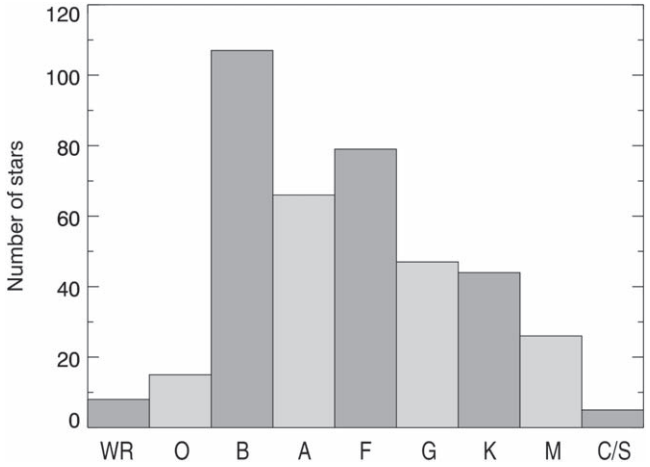

Figure 1. Distribution of stellar spectral types in the UVES-POP library. Spectral type identification was done mostly using the SIMBAD database (Wenger et al. 2000) or, in rare cases, based on stellar atmospheric parameters (see Section 4).

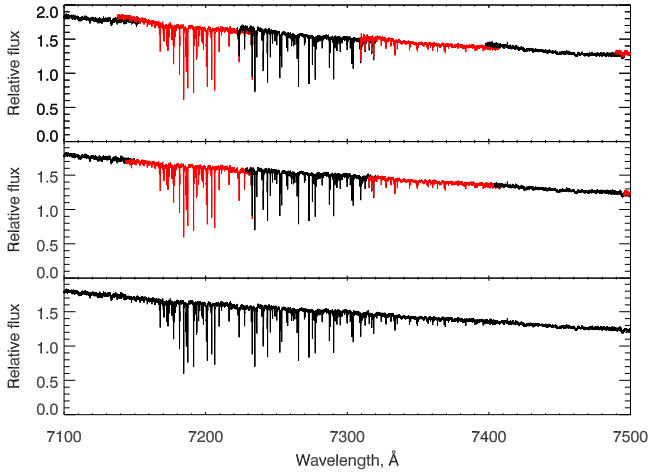

Figure 2. The process of echelle order merging. Top: raw orders before applying corrections for blaze shift and scattered light. Middle: orders after correction. Orders are highlighted in black or red for visualization purposes. Bottom: spectrum after merging of the corrected orders.

Table 2
List of UVES Setups and Wavelength Coverage

Dichroic (Short Name)	Wavelength Range (nm)
DIC1 346 blue arm (346B)	304–388
DIC2 437 blue arm (437B)	373–499
DIC1 580 red arm L (580L)	476–577
DIC1 580 red arm U (580U)	584–684
DIC2 860 red arm L (860L)	660–854
DIC2 860 red arm U (860U)	866–1040

wavelength calibration. The typical offset in UVES is one-twentieth of a pixel (Dekker et al. 2000), but it can be larger than that in some cases. The second main possible reason for the existence of ripples in the final spectra is the inaccurate estimation of scattered light and/or of the sky background. Indeed, many observations in UVES-POP were carried out in twilight. Any over- or undersubtraction of light will lead to the artificial "bending" of spectral orders in flux. The top panel of Figure 2 illustrates how spectral orders look as a result of both effects.

We developed an algorithm that allows us to get rid of ripples or significantly reduce their amplitude. The basis of the algorithm is a nonlinear minimization of χ^2, computed as

$$\chi^2 = \sum_i \frac{(F_i^l - F_i^r)^2}{\sigma_i^{l^2} + \sigma_i^{r^2}}, \quad (1)$$

where $F^{l,r}$ and $\sigma^{l,r}$ are fluxes and their errors from the "left" and "right" overlapping orders, respectively. The algorithm finds the values of the shift and over- or undersubtracted scattered light $\Delta_{\rm sl}$. As an initial guess, we assumed that $\Delta_{\rm sl}$ is proportional to the mean value of flux in the two adjacent orders, which allows us to take into account scattered light. Our tests have demonstrated that in most cases scattered light is oversubtracted. After the determination of both values, we corrected the blaze for both of the previously mentioned effects.

The blaze shift procedure is further complicated by the presence of fringes at wavelengths $\lambda \gtrsim 6700$ Å. The top panel of Figure 3 shows fringes on a raw frame. The fact that fringes

Table 3
The Photometric Bands Used for Spectrophotometric Correction and Some of Their Properties

Band	Phot. Sys.	$\lambda_{\rm eff}$ (Å)	Band	Phot. Sys.	$\lambda_{\rm eff}$ (Å)
B_p	Gaia	5044.4	$P_{\rm vil}$	Vilnius	3768.9
R_p	Gaia	7692.2	$X_{\rm vil}$	Vilnius	4051.3
TB	Tycho	4220.0	$Y_{\rm vil}$	Vilnius	4649.7
TV	Tycho	5266.4	$Z_{\rm vil}$	Vilnius	5151.9
AA_B	WBVR	4347.2	$V_{\rm vil}$	Vilnius	5432.4
AA_V	WBVR	5442.2	$S_{\rm vil}$	Vilnius	6500.3
AA_R	WBVR	7008.8	$Z_{\rm vis}$	VISTA	8762.4
37	13-color	3774.8	$Y_{\rm vis}$	VISTA	10184.2
40	13-color	4046.9	U	Johnson	3663.6
45	13-color	4586.3	B	Johnson	4360.0
52	13-color	5180.2	V	Johnson	5445.8
58	13-color	5806.2	RC	Cousins	6358.0
63	13-color	6349.1	IC	Cousins	7829.2
72	13-color	7222.7	g	SDSS	4673.0
80	13-color	7993.6	r	SDSS	6142.0
86	13-color	8577.7	i	SDSS	7459.0
99	13-color	9813.8			

are strictly fixed in position makes the problem even more complicated. We solved it by decomposing the blaze into two components: the "real blaze" component and a fringe pattern (bottom panel of Figure 3). We defined the real blaze component as a B-spline approximation to the observed blaze, whereas the ratio of the blaze to this B-spline ($A_{\rm fig3} = F_{\rm blaze}/F_{\rm bspline}$) shows the position and the amplitude of the fringes. The B-spline was shifted by the computed value and then multiplied by $A_{\rm fringes}$ in order to restore the fringe pattern.

With all the orders corrected, we proceeded to merge them into one spectral segment. In the overlapping regions, the flux was averaged with weights proportional to the value of $1/\sigma^2$ (flux uncertainty) and normalized to unity. Because of that, the signal-to-noise ratio (S/N) in these regions is approximately $\sqrt{2}$ times higher. The process of ripple correction and order merging is shown in Figure 2.

The described ripple correction algorithm cannot be used in the reddest (860U) segment because echelle orders do not overlap. For

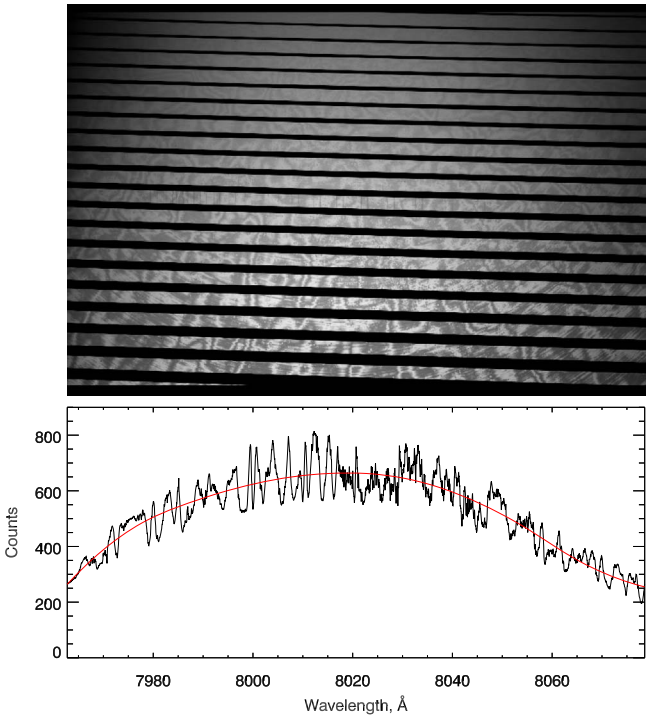

Figure 3. Top: raw UVES spectral flat field in the 860L segment with strong fringes. Bottom: a single flat-field order with fringes. The red line shows the best-fitting B-spline, which we considered as the blaze function approximation.

this reason, the correction in this segment was carried out manually by the optimal selection of parameter values. There was no degeneracy of the two parameters (i.e., the value of the blaze shift and the value of over- or underestimation of scattered light) because the blaze shift and inaccurate subtraction of scattered light affect the orders differently: a blaze shift "tilts" an order, while inaccurate subtraction of scattered light "bends" it.

3.3. Telluric Correction

Observations made with ground-based telescopes suffer from absorption through Earth's atmosphere which leads to telluric lines imprinted on astronomical spectra. In the wavelength range of UVES, there are absorption bands that mostly originate from water vapor and molecular oxygen. There are also two wide ozone bands. Correction of the spectra for telluric absorption is crucial during data processing.

Telluric correction requires accurate wavelength calibration. This means that the positions of telluric lines and other features in the spectra must precisely match the theoretically computed model telluric lines. For this reason, the barycentric and topocentric corrections were here performed after the telluric correction because telluric features should not be shifted by radial velocity effects.

To perform the telluric correction, we need to know how much flux was absorbed on its way through Earth's atmosphere. Spectra can be corrected by dividing the original stellar spectrum by a transmission curve, which can be obtained via one of two methods. The first method is to solve the radiative transfer equation of Earth's atmosphere numerically. The second method is to extract the transmission curve based on the spectrum of a star that has as few spectral features as possible. Usually, fast-rotating A0V stars are observed during the night. However, in our case there are no such observations, so we chose to calculate the transmission curve.

We used the Cerro Paranal Advanced Sky Model by ESO (SkyCalc; Noll et al. 2012; Jones et al. 2013) to produce a grid of Earth's atmosphere transmission curves in the parameter space of air mass ranging from 1.0 to 2.5 with a fixed step of 0.1 and precipitable water vapor (PWV) in the range 0.5–20 mm with increasingly large steps. Our telluric correction procedure approximates an observed stellar spectrum by a linear combination of synthetic stellar templates from the PHOENIX (Husser et al. 2013) and BT-Settl (Allard et al. 2012) libraries using the full-spectrum fitting technique. The templates are shifted by the radial velocity amount $v_{\rm rad}$, broadened according to a projected rotational velocity $v \sin i$, multiplied by a grid of Earth's atmospheric models parameterized by air mass and PWV, and then convolved with the spectrograph's line-spread function (LSF). We use a multiplicative continuum to account for the global difference between flux-calibrated models and uncalibrated stellar spectra. The air mass, PWV, $v_{\rm rad}$, $v \sin i$, and LSF parameters are fitted nonlinearly; the multiplicative polynomial continuum parameters and the weight of the stellar templates in the linear combinations are minimized linearly at each step of the nonlinear minimization. Then, telluric absorption was removed by dividing the original spectrum by the telluric model corresponding to the computed values of air mass and PWV and convolved with the LSF. Since the strongest telluric bands are located in the 860L and 860U segments, air mass and PWV values were computed by fitting these segments, and these values were then fixed when fitting the remaining segments. Note that the advantage of this telluric correction method is that it can also be applied for fitting galaxy and star cluster spectra.

Unfortunately, the quality of telluric correction is rather poor at the full spectral resolution. It might be caused by either improper centering of a star on the slit during observation or an imperfect correction of the atmospheric dispersion. Another factor might be the insufficient quality of Earth's atmosphere transmission models (e.g., incomplete molecular line lists or transition probabilities), leading to similar effects; however, there have been no serious issues reported in the literature when using SkyCalc on full-resolution UVES spectra obtained through a fiber input. All UVES-POP stars were observed through a slit; therefore, the atmospheric seeing quality could have a strong effect on the final spectral resolution if the slit were too wide (which was not often the case because of the narrow $0\farcs5$-wide slit used in the observations). But even subtle seeing variations would cause the effective spectral resolution change and lead to artifacts in the telluric correction. Because of this, the quality of telluric correction of the spectra with the original resolving power $R = 80{,}000$ is often unsatisfactory in the regions of high absorption (see Figure 4, top panel).

At the same time, at the reduced resolving power of $R = 20{,}000$ the telluric correction quality is excellent, and this spectral resolution is sufficient for most applications. It fully covers the needs of stellar population synthesis: $R = 20{,}000$ corresponds to the instrumental resolution of $\sim$6.4 km s^{-1}, which is significantly smaller than the typical velocity dispersion of galaxies or most globular clusters. The middle and bottom panels of Figure 4 demonstrate the telluric correction for HD 162305 in two different spectral segments. Although the quality of the telluric correction at the reduced resolution is good, there are some artifacts because of imperfect

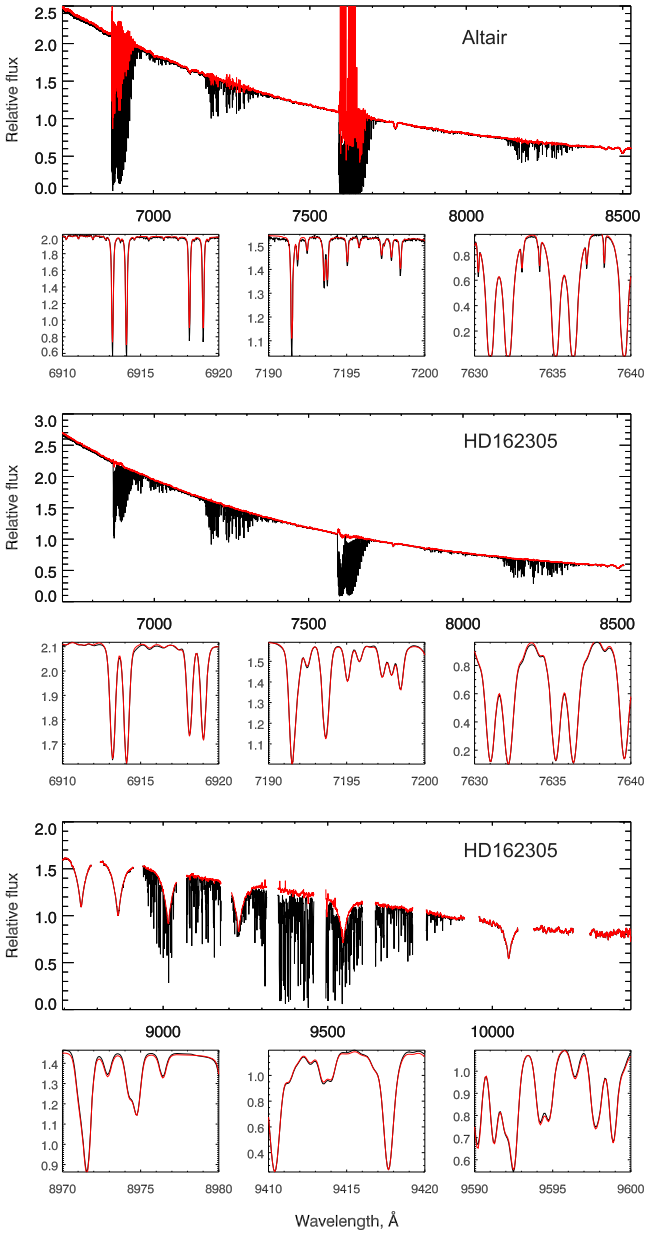

Figure 4. Top: full-resolution ($R = 80{,}000$) spectrum of Altair (the 860L segment) before (black) and after (red) the telluric correction. The three smaller panels show the spectrum in three different spectral ranges with the best-fit Earth atmospheric model (red). Middle and bottom: the same as in the top panels, but for HD 162305 with $R = 20{,}000$.

atmospheric transmission models; the most noticeable artifact is at ~7600 Å, looking like a small bump.

The main release of our recalibrated data set presented here and available via interactive web-based visualization tools was obtained by convolving the original $R = 80{,}000$ spectra with a Gaussian LSF corresponding to $R = 20{,}000$. From now on in this manuscript, we will be dealing with the spectra having a reduced resolving power of $R = 20{,}000$ unless noted otherwise. We also provide full-resolution spectra for download through the website and Virtual Observatory access mechanisms (see Section 5).

3.4. Obtaining UVES Response Curves

After performing the telluric correction, spectra need to be flux-calibrated. Since the original spectra taken with UVES are not ripple and telluric corrected, the original response curves[11] that were derived based on these spectra (see Hanuschik 2003) sometimes have poor quality. We decided to recompute the response curves using the corrected spectra.

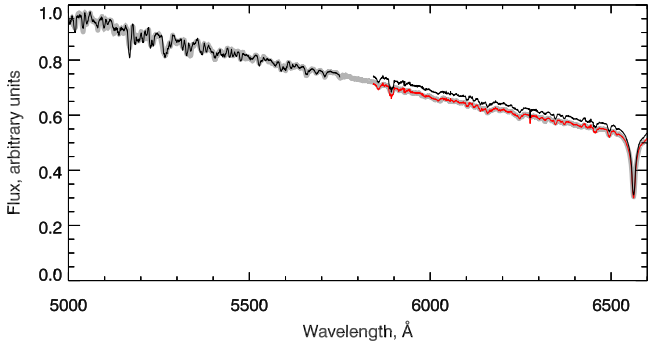

Figure 5. Merging of nonoverlapping spectral segments for Altair. The black line shows the spectra prior to merging. The red line shows the right segment renormalized by the merging procedure. A synthetic spectrum used for the merging of nonoverlapping segments is shown in gray.

As a preparation for this stage, we performed a preliminary determination of stellar atmospheric parameters (see Section 4) using spectra corrected with original response curves that were accurate enough for this purpose. The response curves changed several times over the entire period of observation of UVES-POP owing to mirror recoating or cleaning and filter replacement. Thus, we need to derive response curves for each period of time, i.e., the time interval between two successive changes in the optics of the telescope or the spectrograph. The dates of these changes are documented and presented on the web page of the European Southern Observatory. For each period, we selected stars that have a relatively small number of spectral lines and for which the fitting quality was very good.

For the selected stars, we obtained model spectra corresponding to the atmospheric parameters of these stars. Model spectra were artificially "reddened" by the value of color excess $E(B-V)$ taken from the literature using the extinction law from Fitzpatrick (1999). The response curves were defined as B-splines, which fit the ratios of model spectra to the observed ones. Parts of spectra that could not be adequately described by models were masked out.

3.5. Merging of UVES Spectral Segments

A full spectrum obtained with UVES consists of six segments, some of which overlap. There are also two gaps, one between the segments 580L and 580U and another one between the segments 860L and 860U. The three segments 346B, 437B, and 580L and the two segments 580U and 860L can be merged into two long segments of 255 and 268 nm, respectively. Thus, we used two different merging techniques, one to stitch overlapping segments and the other one to stitch nonoverlapping ones.

In the case of overlapping segments, we calculated the flux in the overlapping regions as the weighted mean of the fluxes of the two segments. Weights were determined as coefficients that linearly increase from 0 at the edge of a segment to 1 within the overlapping region. To merge nonoverlapping segments, we developed an algorithm using synthetic spectra (PHOENIX, Husser et al. 2013; BT-Settl, Allard et al. 2012)

[11] http://www.eso.org/observing/dfo/quality/UVES/qc/SysEffic_qc1.html##response

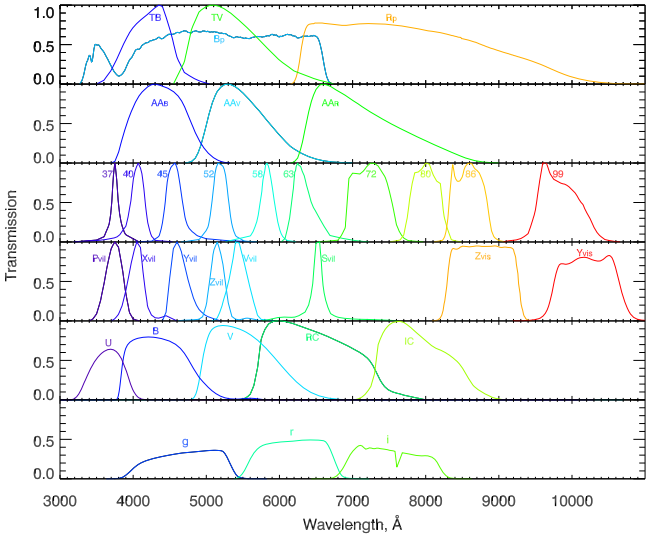

Figure 6. Transmission curves of the photometric bands used for the spectrophotometric correction. Explanation of abbreviations and parameters of the bands are presented in Table 3.

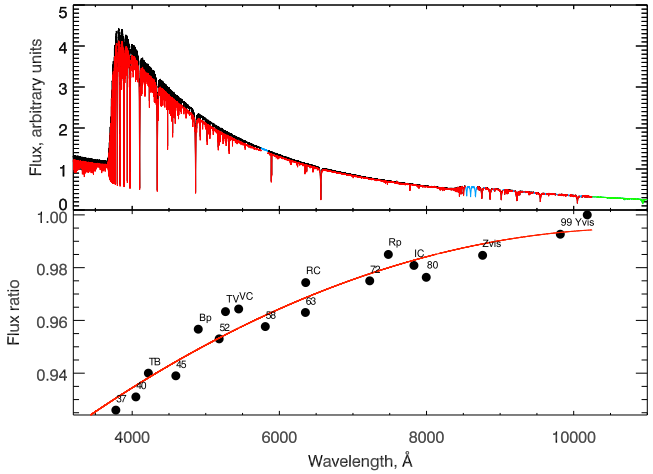

Figure 7. Spectrophotometric correction for the UVES-POP spectrum of HD 75063. Top: spectrum before correction (black line) and after correction (red line). Blue regions demonstrate the best-fitting synthetic spectrum that fills in the gaps, while the green line is an extrapolated spectrum. Bottom: black points are the ratios of observed fluxes from photometric databases and synthetic fluxes computed from the spectrum (the ratios are normalized to the maximal value). The red line is a polynomial fit used for the correction. Explanation of abbreviations and some parameters of the photometric bands are shown in Table 3.

and stellar atmospheric parameters that we obtained by fitting one of the segments (see Section 4). This allows us to estimate the flux difference on both sides of each gap and avoid "steps" in flux in the final spectrum. Figure 5 shows an example of the merging of the nonoverlapping segments.

Before merging, we corrected all spectral segments for Doppler shift caused by barycentric and topocentric velocities. The maximum absolute value of topocentric velocity at the latitude of Cerro Paranal is 423 m s^{-1}, which is especially significant for high-resolution spectra since this value is around 27% of the FWHM at the resolving power of $R = 80{,}000$.

3.6. Variable Stars

Our sample contains 106 variable stars of various variability types: 51 pulsating variables, 14 eruptive variables, 27 rotating variables, 4 eclipsing binaries, and 10 stars of other types. The physics of variability causes changes in the observed radial velocity in the case of pulsating and eclipsing binaries, as well as changes in surface gravity and effective temperature due to stellar pulsations.

We obtained the variability types for these stars and their periods (where applicable and available) from the General Catalogue of Variable Stars (Samus' et al. 2017). For some stars, the periods are not available; however, their published variability type puts limitations on possible period values. We compared the periods of the variable stars of the sample with the differences of starting time between spectral exposures. In all the checked cases for pulsating variables, this difference was much smaller than the period (or typical period) of the corresponding variable stars. Therefore, the different spectral setups were observed in nearly the same variability phase. Thus, the segment merging did not require velocity corrections for individual segments and ensured that the entire spectrum would correspond to the same stellar atmospheric parameters.

We provide the information on stellar variability in the main data table presented in Appendix A and available online.

3.7. Spectrophotometric Correction

Because of varying observing conditions during the night and imperfections of synthetic stellar atmospheres, the response curves obtained as described above when applied to observed spectra of other stars can produce systematic flux calibration uncertainties of up to 20%–30%. Therefore, we performed an additional spectrophotometric correction of the final spectra by using published photometric measurements of the corresponding stars. At the end, we brought the flux scale in the UVES spectra to physical units erg s^{-1} cm^{-2} $Å^{-1}$.

To perform the spectrophotometric correction, we used the broad- and intermediate-band photometric data from Gaia DR2 (Jordi et al. 2010; Gaia Collaboration et al. 2016, 2018), Tycho-2 (Bessell 2000; Høg et al. 2000), the WBVR catalog (Kornilov et al. 1996), the 13-color photometric catalog (Johnson & Mitchell 1975), APASS (Henden et al. 2018), the Cousins catalog (Cousins 1976), and the Vilnius catalog (Boyle et al. 1996), as well as magnitudes in the *Z*-VISTA and *Y*-VISTA bands (Dalton et al. 2006), recalculated from *J* and K_s Two Micron All Sky Survey magnitudes (Skrutskie et al. 2006) using formulae from González-Fernández et al. (2018). The transmission curves of all the photometric filters used in the correction procedure are shown in Figure 6.

First, we converted the data from all catalogs into the Vega system. This was done for the data in the *g*, *r*, and *i* bands of the APASS catalog, which uses the AB system (Oke & Gunn 1983), and data from the Vilnius catalog, which has its own specific photometric system. The magnitudes in the *g*, *r*, and *i* bands were converted to the Vega system using zero-point corrections from Fukugita et al. (1996). We performed the zero-point conversion of the Vilnius data to the Vega system by comparing the Vega magnitudes in this catalog with the value of 0.03^m (Bessell 2005). In addition, we corrected Gaia magnitudes of bright stars that suffered from saturation according to Evans et al. (2018).

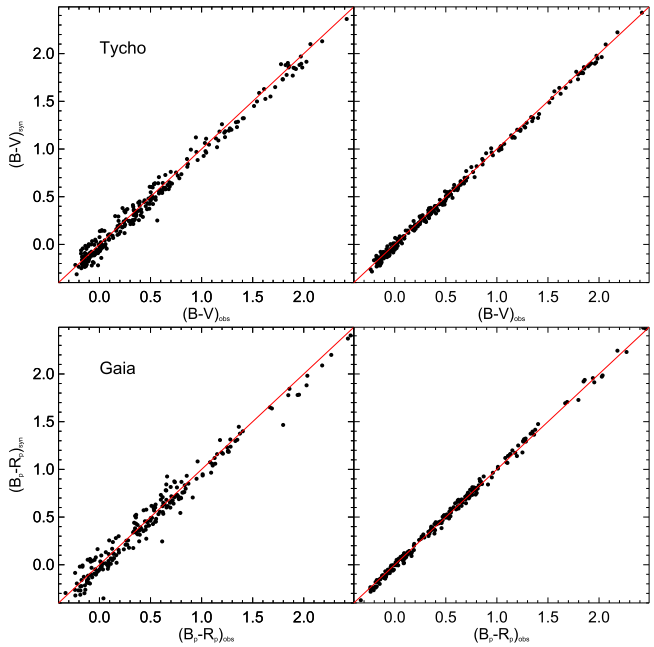

Figure 8. Top: comparison of the synthetic Tycho colors $(B-V)_{\rm syn}$ of the spectra corrected with observed colors $(B-V)_{\rm obs}$ before and after spectrophotometric correction (left and right panels, respectively). Bottom: same as the top panels, but for Gaia colors (B_p-R_p).

To ensure the high quality of the spectrophotometric correction, we need to use the photometric bands with the effective wavelengths covering the entire observed spectral range. It is especially important to use the bands with $\lambda_{\rm eff}$ close to the edges of the UVES spectral range. Because most red filters with $\lambda_{\rm eff} > 9000$ Å have transmission curves that extend beyond the spectral range of UVES, we extrapolated the spectra using best-fitting synthetic stellar atmospheres for the corresponding spectra. This procedure was necessary to use the data in the band Gaia R_p ($\lambda_{\rm eff} = 7418$–9000 Å), Y-VISTA ($\lambda_{\rm eff} = 10184$ Å), and the "99" band of the 13-color catalog ($\lambda_{\rm eff} = 9818$ Å). In addition, we used the same best-fitting stellar templates to fill the gaps between segments and/or individual orders.

The correction algorithm fits a low-order polynomial that transforms an observed spectrum in such a way that the synthetic magnitudes fit the observed ones best. An example of spectrophotometric correction is presented in Figure 7. The algorithm iteratively excludes some data points by using a rejection technique for outliers, which could occur because of high photometric errors or stellar variability. In addition, a wrong cross-match of a star from the UVES-POP list against photometric catalogs could cause these outliers, which is especially relevant for high proper motion stars. In total, we performed spectrophotometric correction for 306 stars from the library.

To check the quality of the spectrophotometric correction, we compared the synthetic colors in the Tycho-2 and Gaia photometric systems with the observed colors. These catalogs contain data for more stars from the UVES-POP library than any other catalog used. In addition, these observations do not suffer from the effects of Earth's atmosphere. Comparison of the synthetic colors of the spectra corrected with observed colors is presented in the Figure 8. Robust standard deviation of the value $(B-V)_{\rm obs} - (B-V)_{\rm syn}$ before the spectrophotometric correction is 0.071 mag, and after the correction it is improved to 0.033 mag; for the Gaia color $(B_p - R_p)$ the corresponding values are 0.085 and 0.034 mag.

3.8. Interstellar Extinction

Calculating interstellar extinction for sources within the Galaxy either requires the knowledge of the three-dimensional dust distribution, known to be strongly nonuniform and notoriously hard to derive, or can be computed using secondary indicators such as interstellar absorption lines of sodium (NaD) or calcium (Ca H and K), which correlate with the line-of-sight amount of dust (e.g., Hobbs 1974; Poznanski et al. 2012).

We computed the color excess $E(B-V)$ for 41 stars using the publicly available code `dustmap`.[12] The algorithm is based on the integration of the extinction along the line of sight using a 3D map of dust in the Milky Way reconstructed from optical-to-near-infrared photometry of stars (Green et al. 2015, 2018). For the remaining 365 stars it was not possible to compute the $E(B-V)$ values because the published 3D map does not cover a substantial portion of the southern hemisphere. We independently determined $E(B-V)$ for 364 stars with the parameters of stellar atmospheres described in Section 4 by approximating the multiplicative continuum returned by the fitting code with the extinction curve from Fitzpatrick (1999).

4. Determination of Stellar Atmospheric Parameters

To use stellar spectra from the recalibrated library for stellar population synthesis, it is crucial to determine the fundamental parameters of stellar atmospheres ($T_{\rm eff}$, $\log g$, [Fe/H], [α/Fe], $v \sin i$). Literature data cover only about half of the stars of the UVES-POP library (Valdes et al. 2004; De Pascale et al. 2014; Soubiran et al. 2016; Worley et al. 2016; Arentsen et al. 2019). Moreover, the measurements are heterogeneous, i.e., determined with different algorithms having different systematic problems that are applied to spectra of varying quality originating from many observing facilities. In addition, the flux recalibration that we performed could change the values of parameters in some stars even if the literature measurements were made on UVES data. Therefore, we decided to determine them for all stars (where possible) using the same technique.

We decided to measure the fundamental stellar parameters fitting the full spectrum against a grid of synthetic stellar atmospheres because all existing grids of empirical stellar spectra have their own systematics related to (i) interpolation of stellar spectra irregularly placed in the parameter space onto a regular grid and (ii) propagation of potentially biased values of parameters from one data set to another, e.g., when parameters of one stellar library (X-Shooter Spectral Library; Arentsen et al. 2019) are based on the calibration obtained from another one (ELODIE 3.1; Prugniel et al. 2007) using a previous version of the calibration of the same method. We also intentionally decided not to use a technique based on the interpolation of spectra in the parameter space to avoid additional uncertainties related to the choice of the interpolation method.

4.1. A Hybrid Minimization Algorithm

High S/Ns, good calibration quality of the reprocessed UVES-POP spectra, and the wide variety of spectral classes require the use of modern high-quality stellar models having as

[12] https://dustmaps.readthedocs.io/en/latest/index.html

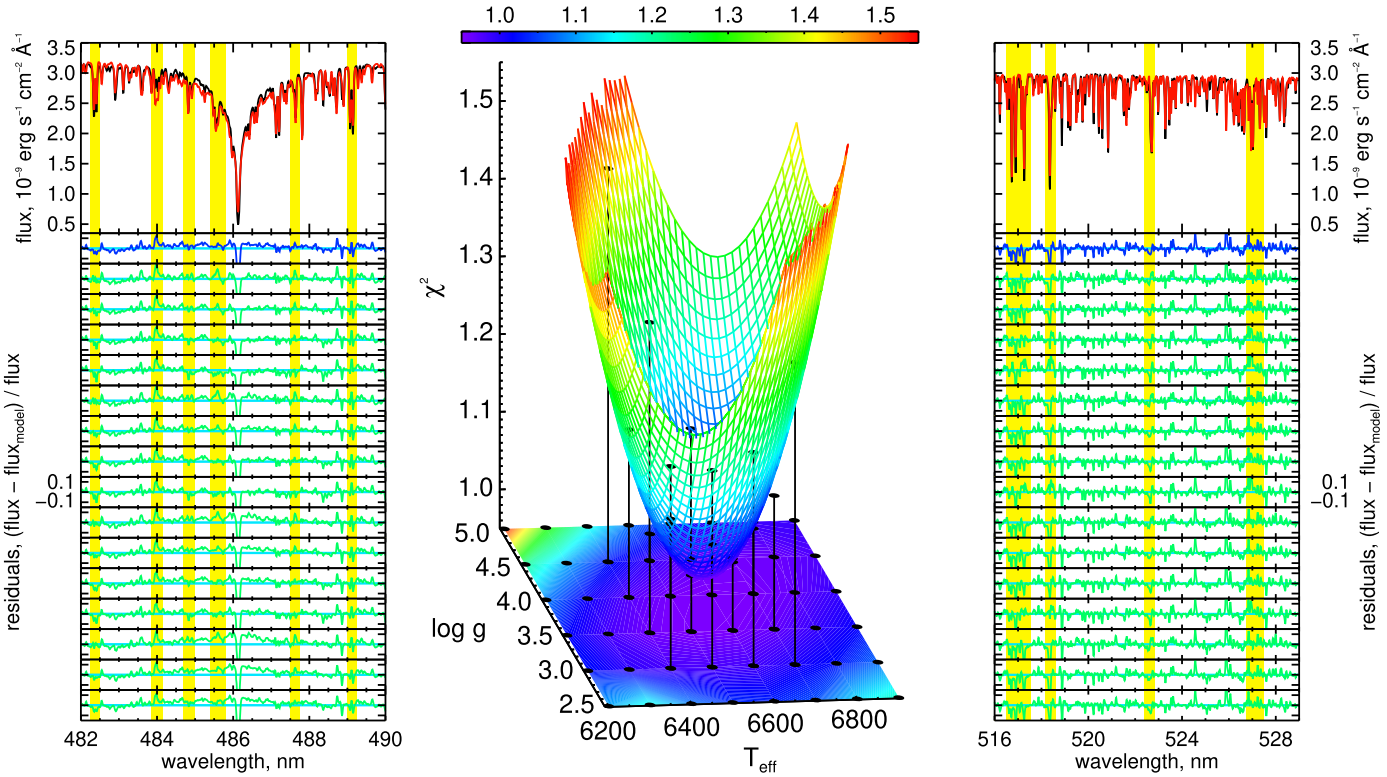

Figure 9. Visualization of the final stage of the minimization method used for the fitting of a spectrum of Procyon by grids of stellar atmosphere models with the two discrete parameters ($T_{\rm eff}$, log g assuming solar metallicity and [α/Fe]) and continuous kinematic parameters ($v_{\rm rad}$, $v \sin i$) and a multiplicative continuum. The middle panel shows a 3D plot of the second-order approximation surface for the χ^2 profile. The projection of the χ^2 profile is shown in the same colors; the black circles mark the grid nodes in which the χ^2 values were calculated. The positions of the nodes selected for the approximation are also shown on a 3D surface. The right and left panels present two small portions of a spectrum around Hβ and the Mg b triplet, their best-fitting models and fitting residuals in every node marked in the middle panel in the decreasing order of $T_{\rm eff}$ and log g. The input data are shown in black, the best-fitting model is shown in red, the residuals are in blue, the residuals in the grid nodes selected for the approximation are shown in green in the same flux scale, and the spectral lines with the most noticeable changes from the parameters of stellar atmospheres are highlighted in yellow.

complete coverage of the parameter space as possible. We chose the PHOENIX synthetic models (Husser et al. 2013) computed over a wide range of values in the parameter space (2300 K $< T_{\rm eff} <$ 15,000 K, $-0.5 <$ log $g < 6.5$, $-4 <$ [Fe/H] < 1 dex for eight different values of [α/Fe] from -0.4 to $+1.2$ dex) and complemented them with the models from the older BT-Settl library (Allard et al. 2012) in the high-temperature (>15,000 K) and low-temperature (<3000 K) regimes. For the BT-Settl models, we fixed [α/Fe] $= 0$ dex. This, however, does not contradict the standard theory of the Galactic evolution because hot (i.e., massive) stars are generally not α-enriched (e.g., Mishenina et al. 2004). The combined grid of models has the full wavelength coverage (300 nm $< \lambda <$ 2500 nm) at the spectral resolution $R = 20{,}000$, but with rather complex and irregular node positions in the four-dimensional parameter space ($T_{\rm eff}$, log g, [Fe/H], [α/Fe]).

The currently available minimization algorithms for finding a solution that can be integrated into a spectrum fitting technique do not handle correctly such complex model grids without interpolation onto a regular grid, which is subject to numerical artifacts. The stellar radial velocity and a projected velocity of rotation, as well as a multiplicative continuum represented by a low-degree polynomial that absorbs potential flux calibration differences between synthetic and observed spectra, also have to be determined.

Therefore, we decided to develop a new hybrid minimization method (Rubtsov et al. 2021) and implemented it as a function in IDL/GDL (the PYTHON implementation is underway). Here we provide a brief description of our approach; its detailed description will be published in a separate paper (E. V. Rubtsov et al., in preparation). The algorithm is designed to work with multidimensional grids of models without interpolation in the process of finding the best-fitting solution. It comprises the two main parts: (i) a hill-climbing part that finds the minimum value of χ^2 at a grid node using the connectivity matrix between the points in the parameter space computed by the triangulation part of the QHULL algorithm (Barber et al. 1996), and (ii) finding the off-node position of the local χ^2 minimum by performing a local approximation of the χ^2 profile by a positively defined quadratic form (Rosen & Marcia 2004). In the second part, a set of nodes (a certain simplex and all nodes associated with it) is selected so that the desired solution is inside the selected simplex. However, if the solution turns out to be outside a given simplex, then it is replaced by an adjacent one in the direction of the obtained solution, and the approximation is repeated. This happens until either the solution is found or the simplices are repeated (i.e., the algorithm loops). In the latter case, the simplices are merged, increasing the region of the parameter space available for finding the local minimum. In the worst-case scenario of a complex shape of the χ^2 profile, the parameters from the first step will be considered to be the solution (and the corresponding flag is returned by the algorithm). This approach allows us to deal with both regular and irregular grids of models, but it can drive solutions into isolated local minima as most local minimization techniques do.

This algorithm works with a discrete set of models distributed in a multidimensional parameter space and does not require interpolation between them. The hybridity consists in using an additional minimizer (in our case MPFIT; Markwardt 2009) to determine independent continuous parameters at the requested grid nodes at each step (thus, the algorithm belongs to the "greedy" class). It also assumes that the continuous parameters determined at every step of the hill-climbing process are not strongly degenerated with those determined discretely. During the full-spectrum fitting of a stellar spectrum, six parameters are simultaneously determined: $T_{\rm eff}$, $\log g$, [Fe/H], and [α/Fe] (discrete), and $v_{\rm rad}$, $v \sin i$, and a multiplicative polynomial continuum (continuous). In this particular case, the discrete and continuous parameters are not pairwise correlated. To illustrate how the method works, Figure 9 shows a simplified version of the fit using two free discrete parameters.

4.2. Stellar Atmospheric Parameters

For all stars in the recalibrated library, we have collected the available information on atmospheric parameters, spectral types, and variability. The resulting data set turned out to be very heterogeneous (45 individual data sources); nonetheless, these data can be used for selection criteria and an initial guess for the spectrum fitting procedure using our technique for the determination of the fundamental stellar parameters.

From the full set of stars in the UVES-POP library (406 stars), we excluded carbon stars (6 C), hot stars with emission lines and very few absorption lines (16 AeBe), and Wolf–Rayet stars (8 W-R). In addition, we excluded spectra consisting of only one atmospheric UV segment 346B (12 spectra). In total, 364 spectra remained in the sample for the determination of the stellar atmospheric parameters.

We fitted 244 of the 364 stars in the wavelength range 380–680 nm, which is relatively well described by synthetic models and allows us to directly compare our results with those obtained in a similar fashion from other empirical libraries of stellar spectra in the same wavelength range (e.g., ELODIE, INDO-US, X-Shooter). For 120 low-temperature stars ($T_{\rm eff} < 4500$ K), high-temperature stars ($T_{\rm eff} > 12{,}000$ K), and stars with missing spectral segments, the fit was carried out in the entire available wavelength range (320–1025 nm). Additionally, to improve the convergence and stability of the fitting, and using assumptions from the stellar physics, we limited the rotational velocity to $v \sin i < 15$ km s^{-1} for giant stars with $\log g < 2.75$. We also generated masks based on the initial guess of the spectral type, which excluded poorly modeled absorption lines in the PHOENIX models (diffuse interstellar bands and helium in hot stars, lithium in cool stars), cores of NaD and Ca H and K lines potentially affected by interstellar absorptions (and chromospheric activity for Ca H and K lines in cool dwarfs), and cores of emission Balmer lines in AeBe stars, which were retained in the spectrum fitting sample and also in cool emission-line giants (Me).

Figure 10 shows several examples of parameter determination using the full-spectrum fitting technique described above for stars having different spectral types and luminosity classes. Figures 11–12 show the projections of the distribution of the obtained parameters $T_{\rm eff}$, $\log g$, [Fe/H], [α/Fe]. Among our sample stars, we found several dwarfs that belong to a rare type of object recently discovered and described in detail in Borisov et al. (2022) referred to as "y-exαfe" stars. These stars have abnormally high [α/Fe] ratios, given their young ages. Following the criteria for the young age $\leqslant 3$ Gyr, and using the available age determination from the literature, we identified nine stars that are very likely "y-exαfe" candidates. Seven of them also have estimates of the eccentricity of their orbits in the Galaxy, which is originally considered as one of the young age indicators. The eccentricities of these stars are low and lie within the range for "y-exαfe" shown in Figure 6 in Borisov et al. (2022). The red line in Figure 12 delineates the locus of "y-exαfe" stars, and the new candidates are shown as four-pointed stars.

Using the stellar atmospheric parameters and luminosities, we estimated stellar masses and ages for 217 stars with the tool SPINS (Lebreton & Reese 2020). To compute luminosities, we applied the same procedure as in Borisov et al. (2022) except for the estimation of bolometric correction, which was computed according to Creevey et al. (2022).

4.3. Comparison with Other Libraries

The largest samples of literature measurement on fundamental stellar parameters for the stars matching our recalibrated UVES-POP list are found in the AMBRE (De Pascale et al. 2014; Worley et al. 2016), PASTEL (Soubiran et al. 2016), and Gaia DR3 (Gaia Collaboration et al. 2022; Recio-Blanco et al. 2022) catalogs, with 123, 174, and 91 stars, respectively (only objects with available measurements counted). We compare our parameters with these data sets in Figure 13. The AMBRE catalog includes only FGKM stars, whereas PASTEL also contains early-type A and B stars. When we compare with the Gaia DR3 data, we exclude stars with $T_{\rm eff}^{\rm Gaia} > 7000$ K since their $T_{\rm eff}$ values show systematic underestimation. One should keep in mind that AMBRE measurements were obtained homogeneously by applying the same data analysis technique to UVES, HARPS, and FEROS archival data, while PASTEL is a literature compilation. Our $T_{\rm eff}$ measurements show good agreement with the literature data: the relative $\mathrm{rms}_{T\rm eff}$ values are around 3.9% when comparing with AMBRE, ~4.2% for PASTEL, and ~4.8% for Gaia DR3. Comparison of $\log g$ gives the following values: $\mathrm{rms}_{\log g}^{\rm AMBRE} = 0.62$ dex, $\mathrm{rms}_{\log g}^{\rm PASTEL} = 0.32$ dex, and $\mathrm{rms}_{\log g}^{\rm Gaia} = 0.51$ dex. Finally, we compared metallicities of stars: $\mathrm{rms}_{\rm [Fe/H]}^{\rm AMBRE} = 0.30$ dex; however, such a high value is caused by a large discrepancy for giants/supergiants with low values of $\log g$. If we consider only stars with $\log g \geqslant 3$, the agreement improves drastically: $\mathrm{rms}_{\rm [Fe/H]}^{\rm AMBRE} = 0.16$ dex. For PASTEL, $\mathrm{rms}_{\rm [Fe/H]}^{\rm PASTEL} = 0.20$ dex; however there is a systematic shift of ~ -0.17 dex. Comparison with Gaia gives approximately the same level of agreement: $\mathrm{rms}_{\rm [Fe/H]}^{\rm Gaia} = 0.19$ dex.

An important factor that might affect the comparison is variability of stars. We have already provided some statistics on them in Section 3.6. In Figure 13 we show pulsating variables as squares and note that they might change their parameters significantly owing to variations of $T_{\rm eff}$ and $\log g$.

We have also compared calibrated flux densities in our spectra with those from the spectral libraries NGSL (Gregg et al. 2006), X-Shooter DR3 (Verro et al. 2022), and ELODIE 3.1 (Prugniel & Soubiran 2004). We cross-matched our list of stars with these three libraries and found 12, 8, and 25 stars in common with each of them, respectively. For comparison purposes, we matched the spectral resolution of the spectra being compared by convolving one of them with a Gaussian with the width corresponding to the quadratic

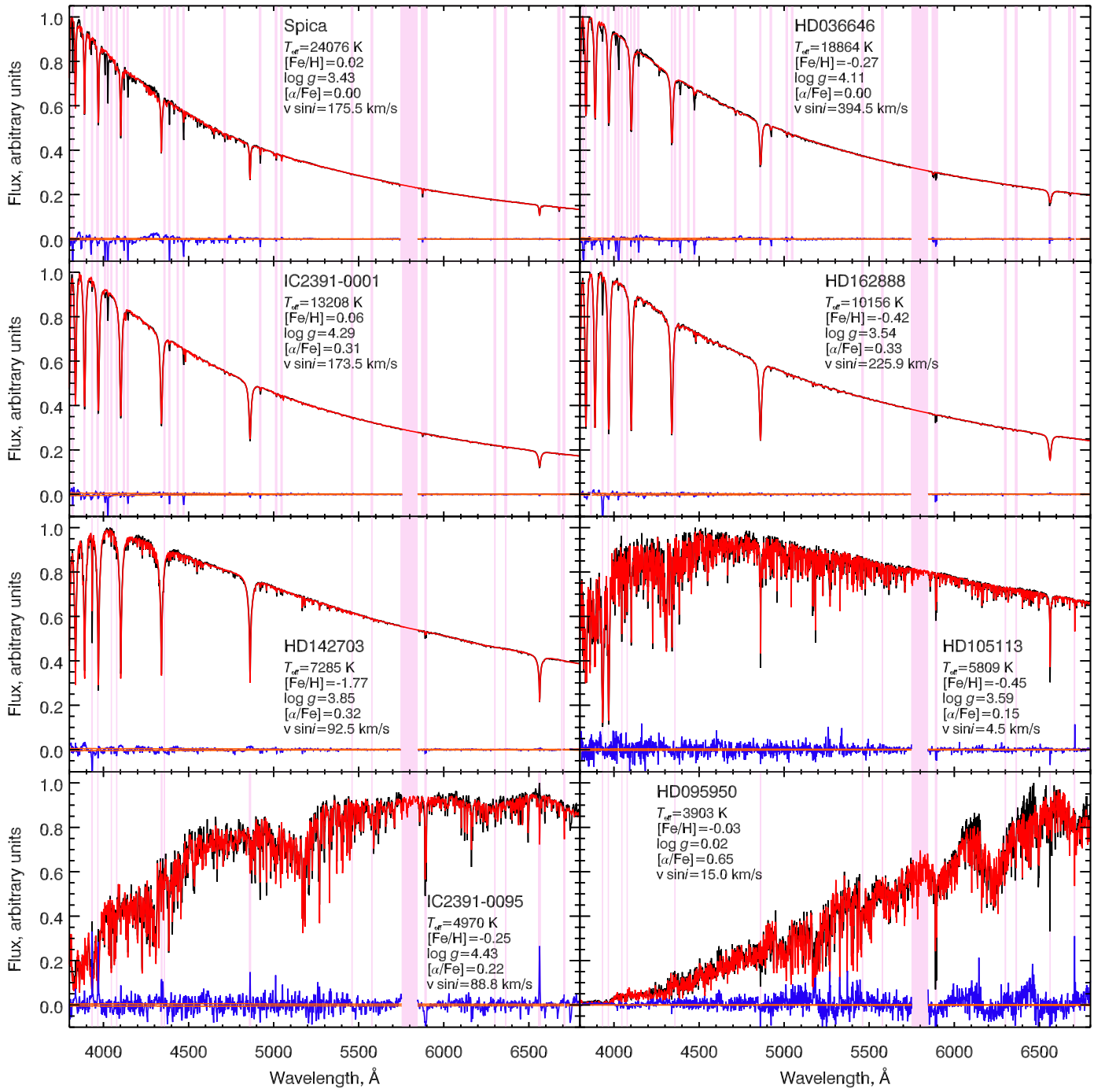

Figure 10. Examples of full-spectrum fitting of stellar spectra. The observed spectra are shown in black in the fitting range from 3800 to 6800 Å, the uncertainties are in orange, the best-fitting models are in red, and the fitting residuals are in blue. Pink-shaded areas denote the masked regions excluded from the fit.

difference of the spectral resolution values. Figures in Appendix B demonstrate the results of the comparison.

We emphasize the comparison with NGSL, which contains spectra collected with the Space Telescope Imaging Spectrograph (STIS) operated at the Hubble Space Telescope. This library has excellent quality of flux calibration because of the location of the telescope outside Earth's atmosphere. Figure 17 demonstrates excellent agreement of 1.0%–3.5% in 10 stars out of 12. The worst agreement is in HD 102212, which is a Mira-type long-period pulsating variable; therefore, the discrepancy can occur from the observations being collected at different pulsation phases. Surprisingly, another long-period variable, HD 206778, shows very good agreement between the two spectral libraries. For HD 47839 (and much less obvious for HD 63077 and HD 76932) we see a disagreement in the atmospheric UV part bluer of the Balmer break: we suspect that the origin of this problem is in the imperfect sensitivity curve determination and flux calibration, which uses tabulated atmospheric extinction coefficients for Paranal, which might change significantly at short wavelengths. We also note that two stars, HD 111786 and HD 142703, are δ Sct–type pulsating variables, which might explain the spectral

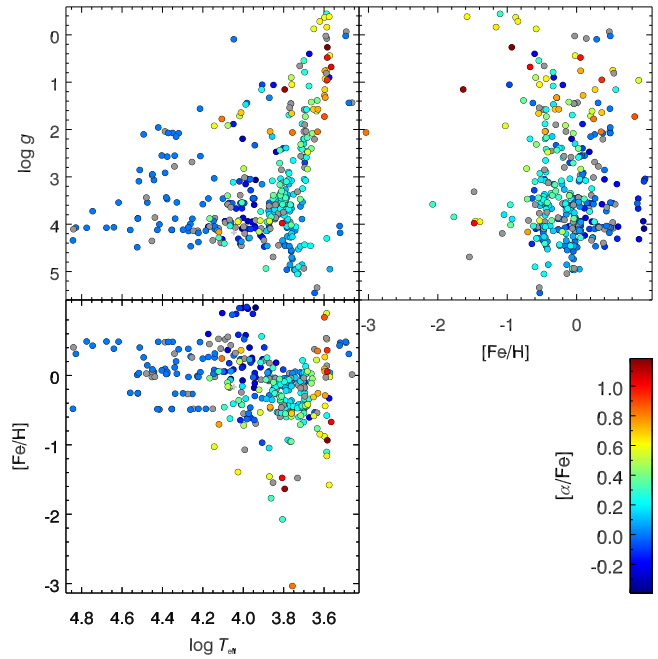

Figure 11. $T_{\rm eff}$, [Fe/H], and log g coverage of the UVES-POP stellar library with [α/Fe] color-coded. The points in gray show the stars for which [α/Fe] was not determined.

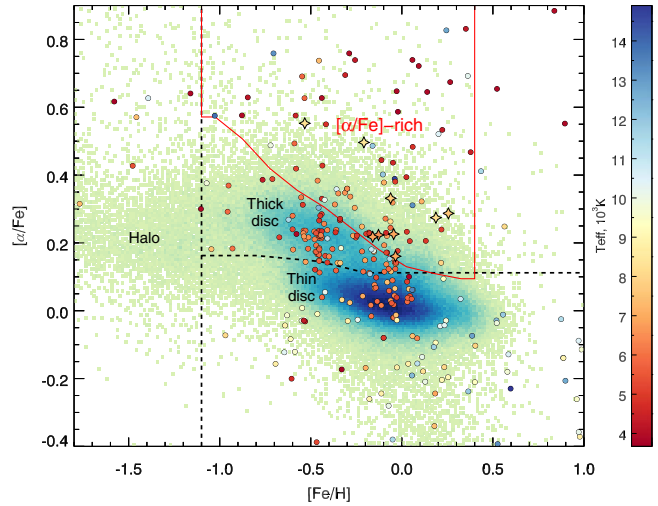

Figure 12. Positions of the UVES-POP stars in the [α/Fe]–[Fe/H] plane with $T_{\rm eff}$ color-coded. Only the stars with [α/Fe] determined in our study are shown. The underlying number density plot shows positions of stars from the third release of the GALAH survey (Buder et al. 2021), with the high S/N and quality criteria for both [α/Fe] and [Fe/H] applied to the input catalog. The black dashed line shows a separation between thin and thick disks obtained by considering the bimodal [α/Fe] distribution at different [Fe/H], which will be described in detail in S. B. Borisov et al. (in preparation), where the authors also assume that objects of the Galactic halo have [Fe/H] $\leqslant -1.1$ dex. The red solid line delineates the area that contains extremely [α/Fe]-rich stars (see Section 4.2); the candidate "y-exαfe" stars are shown as four-pointed stars.

differences in the region containing many high-order log g-sensitive Balmer lines. There is another variable star, HD 22049, of the BY Dra type (i.e., spotted late-type dwarf) that does not exhibit substantial spectral differences between UVES-POP and NGSL. In Table 4, we present the mean relative rms for each spectral segment of UVES spectra compared to NGSL from all 12 stars (second column) and from 11 stars excluding HD 102212 (third column).

Table 4
Mean Values of the Relative rms of Flux Difference between UVESs-POP and NGSL for Each Spectral Segment

Dichroic	$\langle {\rm rms}_{12} \rangle$	$\langle {\rm rms}_{11} \rangle$
346B	4.3%	3.5%
437B	2.0%	2.0%
580L	1.8%	1.8%
580U	1.1%	1.0%
860L	1.1%	0.8%
860U	2.4%	1.8%

Note. The second column ($\langle {\rm rms}_{12} \rangle$) presents the values computed for all 12 matching spectra; the long-period variable HD 102212 was excluded while computing the values presented in the right column ($\langle {\rm rms}_{11} \rangle$).

In the case of the XSL DR3 library, we compared our spectra with the second spectral segment of their spectra (the so-called VIS arm, 5400–10200 Å; see Verro et al. 2022 for details). This comparison shows a somewhat worse agreement (Figure 18), especially in the blue end of the spectral range affected by the "wavy" throughput of the dichroic mirror, which, however, is masked in the merged X-Shooter spectra presented in the public release.

Comparison with ELODIE 3.1 (Figure 19) shows the worst agreement among the three aforementioned libraries. We can see relatively good correspondence in the center of the range; however, in many cases, there is a strong "bending" of flux at the edges, especially in the blue part.

Neither X-Shooter nor ELODIE used broad- and/or intermediate-band photometry to correct the global shape of the spectra. We therefore attribute the disagreement to these stellar libraries rather than to our collection of spectra.

While we were finalizing the work on this paper, the Gaia Collaboration released low-resolution BP/RP spectra as part of DR3 (Gaia Collaboration et al. 2022; Montegriffo et al. 2022). A total of 302 stars from our sample have Gaia BP/RP spectra, which we directly compared with our data. We first convolve UVES spectra with the LSF of Gaia BP/RP spectra (see Figure 17 in Montegriffo et al. 2022) varying across the wavelength. One should keep in mind that because of the extreme difference in spectral resolution, the convolution kernel is very broad and might cause edge effects in the comparison. Then, we bin the convolved spectra in the spectral segments, which correspond to spectral pixels in Gaia data. Finally, we directly compare the spectral flux densities in each pixel. In Figure 14 we compare resolution-degraded UVES spectra with BP/RP spectra from Gaia DR3 for several stars. While for many spectra the overall continuum shape matches between two sources (Figure 14, left six panels), about one-third of the BP/RP spectra display strong continuum artifacts, the most frequent being moderate to strong "dips" in the red end of the BP Gaia segment at $\lambda = 500$–670 nm (Figure 14, right six panels). This likely indicates an issue in the spectrophotometric calibration of Gaia low-resolution spectra because none of the other sources with which we compared UVES spectra display similar features. Besides, in the majority of Gaia BP/RP spectra, even when the overall continuum shape matches that of UVES spectra, we see high-frequency "waves" (peak-to-peak distance of $\sim$20 nm) with amplitudes reaching 20%. Therefore, we conclude that at present one should not use Gaia DR3 BP/RP spectra as tertiary spectrophotometric standards to

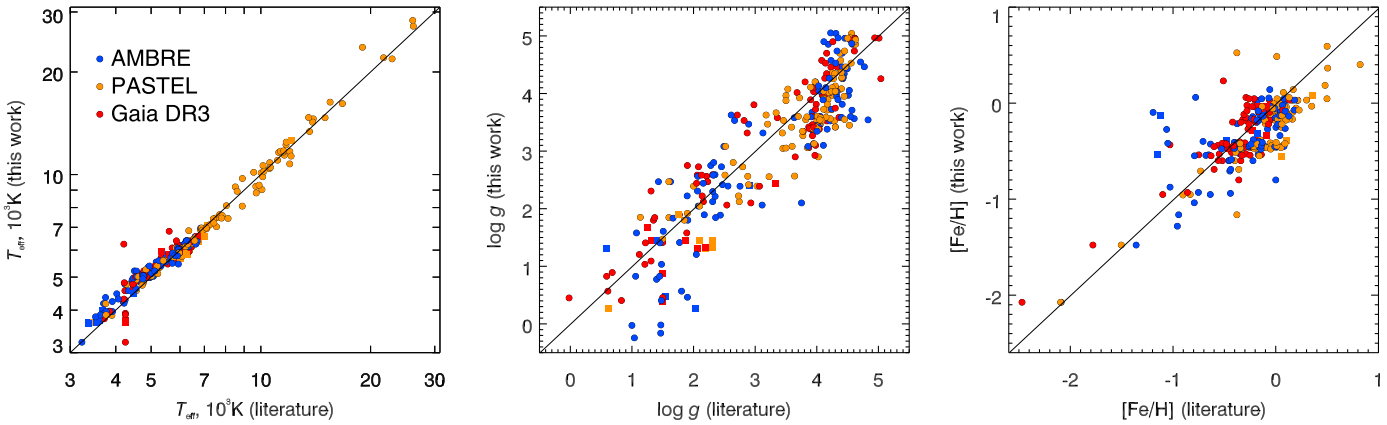

Figure 13. Comparison of atmospheric parameters $T_{\rm eff}$, log g, and [Fe/H] between this work and the literature. Stars that are presented in more than one catalog are shown multiple times. Pulsating variable stars are marked by squares.

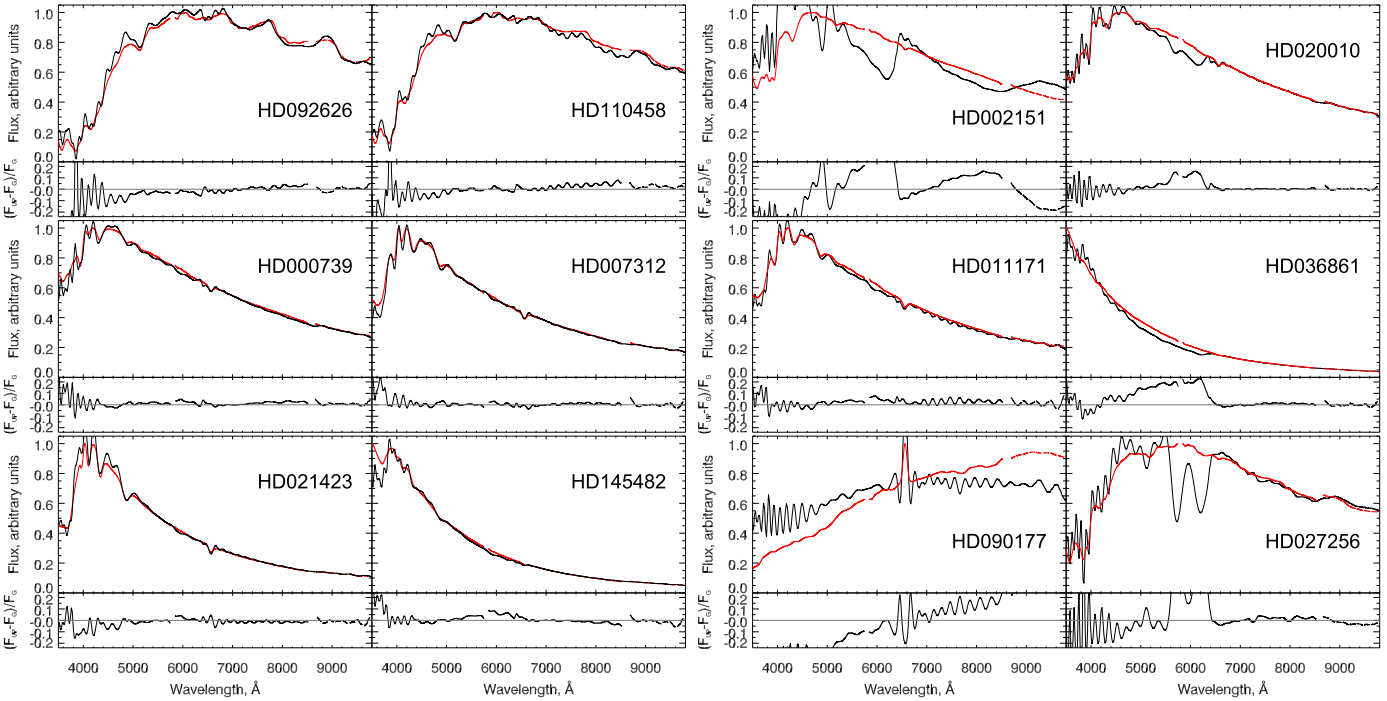

Figure 14. Examples of 12 resolution-degraded UVES-POP spectra (red) with Gaia BP/RP spectra (black) overplotted. All spectra are normalized to unity at the maximal flux of the convolved UVES-POP spectrum. Below each plot we show a panel with the fractional flux differences between the two spectra. The left six panels present the stars with a satisfactory agreement between UVES-POP and Gaia; the right six panels show stars with obvious calibration issues in the Gaia BP/RP spectra. None of the 12 stars have significant variability according to SIMBAD.

perform flux calibration of higher-resolution spectra. Hopefully, these spectrophotometric calibration issues will be corrected in the next Gaia Data Release.

5. Web Service for Data Access and Quality Control

We publish the results of the recalibration and analysis of the spectra in the UVES-POP library in the dedicated website of the VOXAstro Stellar Libraries project: https://sl.voxastro.org/library/UVES-POP/details/. We created a user-friendly modern and interactive web interface for accessing and visualizing data. The server-side part of the application uses Python-based framework Django[13] on top of the PostgreSQL database. The interactive front-end part of the application was developed using JavaScript framework Vue.js[14] and Plotly.js library,[15] which allows us to efficiently display high-resolution spectra. A screenshot of this tool with a spectrum of HD 162889 is shown in Figure 15.

In the top section of the web page, there are links to the general description of the library, buttons for downloading all spectra at once in a single archive (see the description of the FITS binary table structure of the output results in Table 5), and/or the table with stellar atmospheric parameters (see Table 6), the latter is also available in a machine-readable version online. An interactive table and figure are also available on the website. This allows one to quickly find an object of interest in the database and sort the results by different

[13] https://www.djangoproject.com/

[14] https://vuejs.org/

[15] https://plotly.com/javascript/

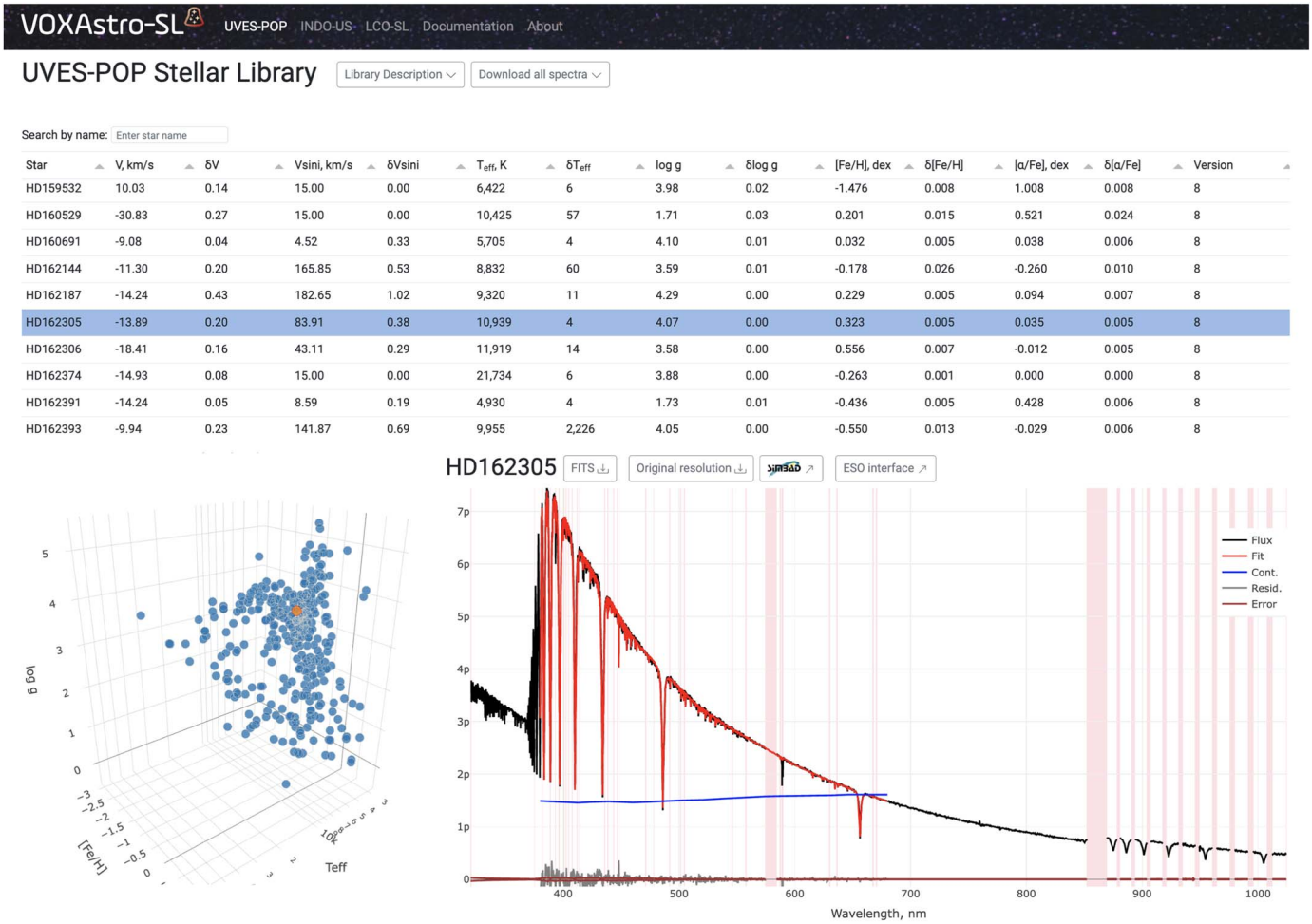

Figure 15. A screenshot of an interactive web-based spectral viewer. An $R = 20{,}000$ spectrum of HD 162305 is shown in black, the best-fitting model is in red, and the multiplicative polynomial continuum is in blue. Pink shaded areas denote the masked regions excluded from the fit.

parameters. This table is related to the 3D visualization of the parameter space for stellar atmospheres in the bottom left part of the page. This interactive 3D plot in the $T_{\rm eff}$, log g, [Fe/H] space displays the results of the full-spectrum fitting of UVES-POP spectra performed by our data analysis technique described above.

Selection of a data point in this plot or a line in the data table above will display a spectrum with its best-fitting results on the bottom right panel of the web page, as well as a download button for that particular spectrum and a link to the SIMBAD database and ESO archive to the data for the corresponding star.

We developed a dedicated password-protected part of the project website to perform (i) quality control for the data reduction, order and segment merging, telluric correction, flux calibration; (ii) assessment of the full-spectrum fitting quality using synthetic stellar atmospheres; and (iii) reliability of the derived stellar atmospheric parameters. Each of the three aspects is graded from 1 (inadequate) to 5 (excellent). Users performing quality control can also leave comments and see a full version history of the recalibration for every star. Most stars in the current release are at version 7. After each iteration of the quality control corresponding to a separate version number, the spectra, which were found to have problems with at least one of the three aspects, were reprocessed. To minimize the subjective factor of the grading, several members of our team were involved in the quality control. At least three persons checked each spectrum (and a majority of spectra were checked by five individuals).

To grade the recalibration quality, a reviewing person had to (i) inspect a spectrum for the presence of residual ripples between echelle orders and flux "steps" between UVES spectral segments, (ii) inspect the regions of strong telluric absorption for strong residuals, and (iii) assess the global spectral shape to detect large-scale flux calibration errors. To grade the full-spectrum fitting quality, one had to (i) inspect fitting residuals in the wings of Balmer lines in intermediate to hot stars, (ii) verify whether Balmer line cores were properly modeled (does not apply to emission-line stars), (iii) check whether molecular bands in cool stars were adequately described by the model, and (iv) check the residuals in several known multiplets of iron and the most prominent absorption lines of α-elements (e.g., Mg b) to assess the quality of the derived iron and α-abundances. Finally, to grade the quality of the stellar atmospheric parameters, one had to check the availability of literature data in the SIMBAD database or at least a spectral type and a luminosity class and conclude whether the derived parameters corresponded to the published spectral type and/or atmospheric parameters. For example, if a star is classified as A5V in the literature and its derived $\log g = 3.0$, it likely indicates a problem.

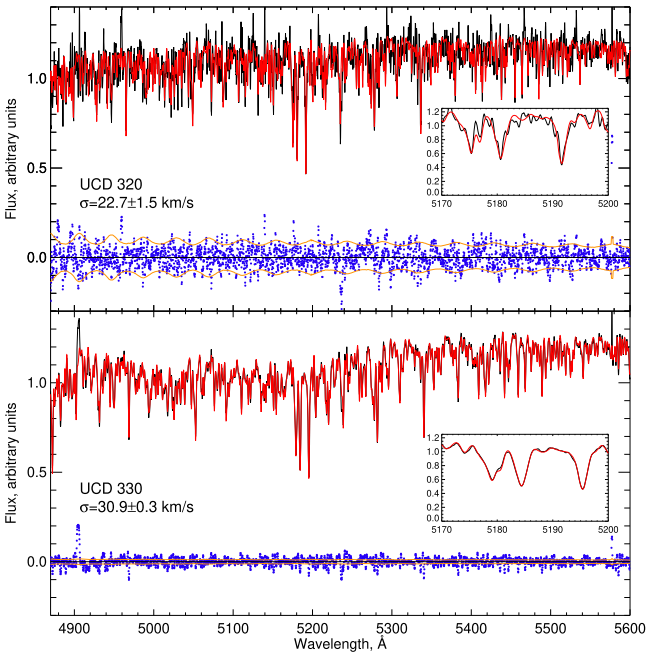

Figure 16. Spectra of UCD 320 and UCD 330 (black) and best-fitting models (red); residuals are shown as blue points. The insets show the spectral region around the Mg *b* triplet. For better visibility, flux errors and residuals for UCD 320 are reduced by a factor of 4.

From the results of the quality control procedure, we conclude that (i) the spectrum recalibration quality is generally very good except for two to three stars where an unknown factor caused the distortion of flux in one of the blue segments; (ii) the full-spectrum fitting quality against a grid of synthetic stellar spectra is the best at subsolar metallicities in the range of 4800 K $< T_{\rm eff} <$ 13,000 K, whereas it deteriorates at lower temperatures and higher metallicities, potentially because of incomplete spectral line lists and/or wrong opacities used in the stellar atmospheric modeling for cool stars, and also at high temperatures, where non-LTE effects become important; and (iii) stellar atmospheric parameters are sometimes biased because of degeneracies, i.e., slightly overestimated $T_{\rm eff}$ leads to significantly overestimated $\log g$, but the use of the novel minimization technique has drastically reduced these effects.

6. Fitting Galaxy Spectra Using UVES-POP Stellar Templates

As an additional test of the quality of the UVES-POP spectral library recalibration, we performed a pixel space fitting of the two ultracompact dwarfs (UCDs) UCD 320 and UCD 330 in the nearby Centaurus A galaxy group in order to estimate their radial velocities and stellar velocity dispersions. Such galaxies typically host old stellar populations (Chilingarian et al. 2008, 2011) often enhanced in α-elements (Francis et al. 2012), in which the prevailing contribution to the total luminosity in the optical domain comes from G and K giants. Although UCDs are usually described by simple stellar populations, they often show color gradients in high-resolution images, which might suggest a radial metallicity gradient (Afanasiev et al. 2018). Therefore, it is reasonable to use several template stars spanning a range of metallicities to infer stellar kinematics of UCDs.

We selected eight recalibrated spectra of G and K giants with the atmospheric parameters lying in the range 4000 K $\leqslant T_{\rm eff} \leqslant$ 6000 K, 1 $\leqslant \log g \leqslant$ 2, and -1 dex $\leqslant$ [Fe/H] $\leqslant$ 0 dex. Spectra of both UCDs obtained with UVES were downloaded from the ESO Archive. These spectra were taken with a 1″ slit and have a resolving power of about $R \approx 42{,}000$. We degraded the spectral resolving power in the UCD spectra to $R = 20{,}000$ to match the recalibrated UVES-POP stellar spectra. This also improved S/Ns in these spectra: the final S/N values after the convolution per pixel are $S/N_{320} \approx 4$ and $S/N_{330} \approx 24$. To estimate radial velocity and velocity dispersion, we used the penalized pixel fitting procedure (pPXF; Cappellari & Emsellem 2004) with a set of eight templates. The values we obtained are $\sigma = 22.7 \pm 1.5$ km s^{-1} and $\sigma = 30.9 \pm 0.3$ km s^{-1} for UCD 320 and UCD 330, respectively. They are in a perfect agreement with Voggel et al. (2018), Rejkuba et al. (2007), and Taylor et al. (2010) (UCD 320) and with Voggel et al. (2018), Rejkuba et al. (2007), and Hernandez et al. (2018) (UCD 330). The results of the spectral fitting for the two UCDs are shown in Figure 16.

7. Summary

We presented the results of reprocessing, recalibrating, and analyzing a data set containing 406 high-resolution stellar spectra with $R = 20{,}000$ and $R = 80{,}000$ from the UVES-POP stellar spectral library. The main goal of this project is to obtain a set of well-calibrated spectra, which can be used for stellar population synthesis. Our results are as follows:

1. We solved the problem of imperfect echelle order matching. The "distortion" of echelle orders in flux space was producing ripples in the regions of the merged spectra where the orders overlap. This prevented the spectra from the original data release from being used for stellar population synthesis.
2. We performed the merging of nonoverlapping spectral segments by using synthetic stellar atmospheres. The original UVES-POP spectra equated the fluxes from each side of the wavelength gaps, leading to "steps" in the overall spectral shape.
3. We performed a telluric correction for all spectra using a dedicated algorithm and a grid of models computed with the ESO SKYCALC tool. This eliminates telluric absorption features produced by oxygen, water vapor, and ozone in Earth's atmosphere.
4. We performed the spectrophotometric calibration of UVES-POP spectra by using nine photometric catalogs, including two catalogs from the Tycho and Gaia space missions. The final spectra are converted into absolute physical flux density units erg cm^{-2} s^{-1} Å^{-1}; fluxes are corrected to above Earth's atmosphere.
5. We estimated interstellar extinction values for 41 stars using 3D dust extinction maps, and for 364 stars $E(B-V)$ values were calculated from the fitting of atmospheric parameters.
6. We matched our sample with the General Catalog of Variable Stars and discussed potential problems of spectral recalibration that may arise from intrinsic variability.
7. We compared the recalibrated UVES-POP spectra for a subsample of stars with the spectra from three other spectral libraries (NGSL, ELODIE, X-Shooter) to conclude that our photometry-based flux calibration approach was successful.
8. For 364 spectra, we computed fundamental stellar atmospheric parameters $T_{\rm eff}$, $\log g$, [Fe/H], and [α/Fe],

as well as radial velocity and rotational velocity ($v_{\rm rad}$, $v \sin i$), using our own full-spectrum fitting technique based on PHOENIX/BT-Settl synthetic stellar atmospheres. The comparison of the derived parameters with published data from the AMBRE and PASTEL catalogs shows good agreement.

9. We presented an example of the usage of the recalibrated UVES-POP spectra by performing full-spectrum fitting of archival UVES spectra of two dwarf galaxies and estimated their stellar velocity dispersion, which happened to agree perfectly with the published values for these two galaxies.
10. All the data and spectrum fitting results are made publicly available from the project website https://sl.voxastro.org/library/UVES-POP/details/, which also provides convenient data visualization tools.

The initial part of this work and spectral recalibration was supported by the RScF grant 17-72-20119; the efforts on the spectrophotometric recalibration were supported by the RScF grant 19-12-00281. I.C.'s research is supported by the SAO Telescope Data Center. S.B., I.C., and K.G. also acknowledge support by the ESO Visiting Scientist Programme. We thank the anonymous referee for the important comments that improved the quality of this paper. We are grateful to Albert Shaykhutdinov (ASC LPI, Russia) for his help with the calculation of topocentric corrections and Patrick de Laverny (OCA, France) for useful comments. This research made use of the SIMBAD database and VizieR catalog access tool, both operated at CDS, Strasbourg, France.

Facility: VLT:Kueyen

Appendix A
Description of the Columns in the Data Tables

In Table 5, we list the columns along with their description of the FITS binary table that contains all spectra and fitting results. Table 6 describes the content of the FITS binary table with stellar atmospheric parameters.

Table 5
Description of the Output Structure of the Spectrum Fitting Results Stored in the Binary FITS Table Format Available on the Website

Column Name	Units	Data Type	Description
objname		string	UVES-POP identifier
wave	nm	double	Array of wavelengths
flux	erg cm^{-2} s^{-1} Å^{-1}	double	Array of flux
error	erg cm^{-2} s^{-1} Å^{-1}	double	Array of flux error
pixmask		long	Array of mask
quality		long	Array of quality flags
swlvec	nm	double	Array of wavelength scale shifts
lsfvec	km s^{-1}	double	Array of LSF velocity and dispersion
model	erg cm^{-2} s^{-1} Å^{-1}	double	Stellar spectrum model from grid
mcont		double	Multiplicative continuum
bestfit	erg cm^{-2} s^{-1} Å^{-1}	double	Best-fit model
method		string	Name of data analysis method
grid_name		string	Name of the model grid used
mdegree		long	Degree of multiplicative polynomial
wlr	nm	double	Wavelength range for fitting
*i*_v	km s^{-1}	double	Initial guess for radial velocity
v	km s^{-1}	double	Radial velocity
*e*_v	km s^{-1}	double	Uncertainty of radial velocity
*i*_vsini	km s^{-1}	double	Initial guess for projection of the rotation velocity
vsini	km s^{-1}	double	Projection of the rotation velocity
*e*_vsini	km s^{-1}	double	Uncertainty of projection of the rotation velocity
*i*_teff	K	double	Initial guess for effective temperature
teff	K	double	Effective temperature
*e*_teff	K	double	Uncertainty of effective temperature
*i*_logg	dex	double	Initial guess for surface gravity
logg	dex	double	Surface gravity
*e*_logg	dex	double	Uncertainty of surface gravity
*i*_fe_h	dex	double	Initial guess for metallicity
fe_h	dex	double	Metallicity [Fe/H]
*e*_fe_h	dex	double	Uncertainty of metallicity
*i*_a_fe	dex	double	Initial guess for α-element abundance
*a*_fe	dex	double	α-element abundance [α/Fe]
e_a_fe	dex	double	Uncertainty of α-element abundance
chisqr		double	χ^2 statistics
dof		long	Number of degrees of freedom
chi2dof		double	Normalized χ^2
mpfit_bestnorm		double	Value of the summed squared weighted residuals
mpfit_dof		long	Computed number of degree of freedom
mpfit_nfev		long	Total number of function evaluations performed
mpfit_nfree		long	Number of free parameters in the fit
mpfit_npegged		long	Number of free parameters that are pegged at a limit

Table 5
(Continued)

Column Name	Units	Data Type	Description
mpfit_niter		long	Total number of iterations completed
mpfit_status		long	Integer status code is returned (see MPFIT description)
mpfit_errmsg		string	String error or warning message is returned (see MPFIT description)
simbad		string	SIMBAD identifier
hd		string	HD identifier
hr		string	HR identifier
hip		string	Hipparcos identifier
tyc		string	Tycho identifier
gaia_dr2		string	Gaia DR2 identifier
gaia_dr3		string	Gaia DR3 identifier
r.a.	deg	double	R.A.
decl.	deg	double	Decl.
date		string	Date of observation (YYYY-MM-DDThh:mm:ss.sss)
exptime	s	double	Total integration time
spclass		string	Spectral class
mass	$M_{\odot}$	double	Stellar mass
*e*_mass	$M_{\odot}$	double	Uncertainty of stellar mass
age	Gyr	double	Stellar age
*e*_age	Gyr	double	Uncertainty of stellar age
ebv	mag	double	Color excess $E(B-V)$ from fit
ebv_err	mag	double	Uncertainty of $E(B-V)$ from fit
ebv_map	mag	double	Color excess $E(B-V)$ from DUSTMAPS (Green 2018)
lit_ref		string	Reference to the literary source of measurements
lit_v	km s^{-1}	double	Radial velocity from literature
lit_e_v	km s^{-1}	double	Uncertainty of radial velocity from literature
lit_vsini	km s^{-1}	double	Projection of the rotation velocity from literature
lit_e_vsini	km s^{-1}	double	Uncertainty of projection of the rotation velocity from literature
lit_teff	K	double	Effective temperature from literature
lit_e_teff	K	double	Uncertainty of effective temperature from literature
lit_logg	dex	double	Surface gravity from literature
lit_e_logg	dex	double	Uncertainty of surface gravity from literature
lit_fe_h	dex	double	Metallicity [Fe/H] from literature
lit_e_fe_h	dex	double	Uncertainty of metallicity from literature
lit_a_fe	dex	double	α-element abundance [α/Fe] from literature
lit_e_a_fe	dex	double	Uncertainty of α-element abundance from literature
variance		long	Variance flag (true/false)
gcvs		string	GCVS identifier
gcvs_n		string	GCVS indicator
gcvs_type		string	Type of variance from GCVS
gcvs_period	day	double	Period of variance from GCVS
gcvs_name		string	Name of variance from GCVS
segments		long	Segment flags
resolution		double	Spectral resolution
phot_name		string	Array of filter names
phot_mag	mag	double	Array of magnitudes in corresponding filters
phot_ref		string	References to filter curves

Table 6
Description of the Structure with the Catalog of Atmospheric Parameters

Column Name	Units	Data Type	Description
objname		string	UVES-POP identifier
simbad		string	SIMBAD identifier
hd		string	HD identifier
hr		string	HR identifier
hip		string	Hipparcos identifier
tyc		string	Tycho identifier
gaia_dr2		string	Gaia DR2 identifier
gaia_dr3		string	Gaia DR3 identifier
url_r20		string	Link to download the spectrum $R = 20{,}000$ with analysis results
url_r80		string	Link to download the spectrum $R = 80{,}000$

Table 6
(Continued)

Column Name	Units	Data Type	Description
r.a.	deg	float	R.A.
decl.	deg	float	Decl.
date		string	Date of observation (YYYY-MM-DDThh:mm:ss.sss)
exptime	s	float	Total integration time
spclass		string	Spectral class
mass	$M_{\odot}$	float	Stellar mass
*e*_mass	$M_{\odot}$	float	Uncertainty of stellar mass
age	Gyr	float	Stellar age
*e*_age	Gyr	float	Uncertainty of stellar age
ebv	mag	float	Color excess $E(B-V)$ from fit
ebv_err	mag	float	Uncertainty of $E(B-V)$ from fit
ebv_map	mag	float	Color excess $E(B-V)$ from DUSTMAPS (Green 2018)
nsegments		long	Number of segments of spectrum
variance		long	Variance flag (true/false)
gcvs		string	GCVS identifier
gcvs_n		string	GCVS indicator
gcvs_type		string	Type of variance from GCVS
gcvs_period	day	float	Period of variance from GCVS
gcvs_name		string	Name of variance from GCVS
v	km s^{-1}	float	Radial velocity
*e*_v	km s^{-1}	float	Uncertainty of radial velocity
vsini	km s^{-1}	float	Projection of the rotation velocity
*e*_vsini	km s^{-1}	float	Uncertainty of projection of the rotation velocity
teff	K	float	Effective temperature
*e*_teff	K	float	Uncertainty of effective temperature
log*g*	dex	float	Surface gravity
e_log*g*	dex	float	Uncertainty of surface gravity
fe_h	dex	float	Metallicity [Fe/H]
*e*_fe_h	dex	float	Uncertainty of metallicity
*a*_fe	dex	float	α-element abundance[α/Fe]
*e*_a_fe	dex	float	Uncertainty of α-element abundance
chi2dof		float	Normalized χ^2
lit_v	km s^{-1}	float	Radial velocity from literature
lit_e_v	km s^{-1}	float	Uncertainty of radial velocity from literature
lit_vsini	km s^{-1}	float	Projection of the rotation velocity from literature
lit_e_vsini	km s^{-1}	float	Uncertainty of projection of the rotation velocity from literature
lit_teff	K	float	Effective temperature from literature
lit_e_teff	K	float	Uncertainty of effective temperature from literature
lit_log*g*	dex	float	Surface gravity from literature
lit_e_log*g*	dex	float	Uncertainty of surface gravity from literature
lit_fe_h	dex	float	Metallicity [Fe/H] from literature
lit_*e*_fe_h	dex	float	Uncertainty of metallicity from literature
lit_*a*_fe	dex	float	α-element abundance [α/Fe] from literature
lit_*e*_a_fe	dex	float	Uncertainty of α-element abundance from literature
lit_ref		string	Reference to the literary source of measurements

(This table is available in its entirety in machine-readable form.)

Appendix B
Additional Figures: Comparison of Recalibrated UVES-POP Spectra with Three Optical Stellar Spectral Libraries

Figures 17–19 demonstrate the results of the comparison of the recalibrated UVES-POP spectra with the spectra from the NGSL, ELODIE, and X-Shooter libraries.

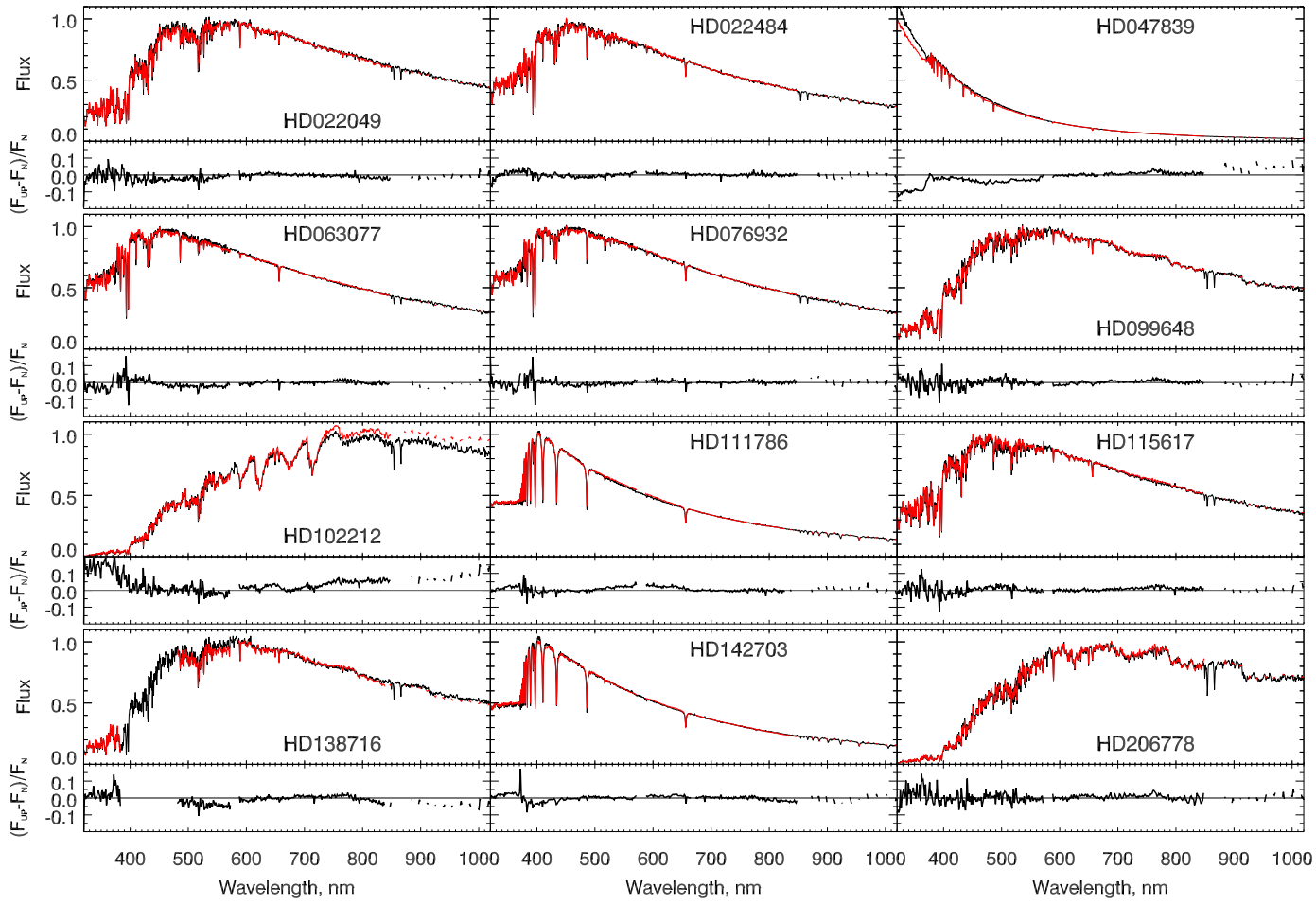

Figure 17. Spectra of 12 stars from UVES-POP (red) and NGSL (black). For comparison purposes, we degraded the resolution of the UVES-POP spectra and applied the same wavelength sampling as NGSL.

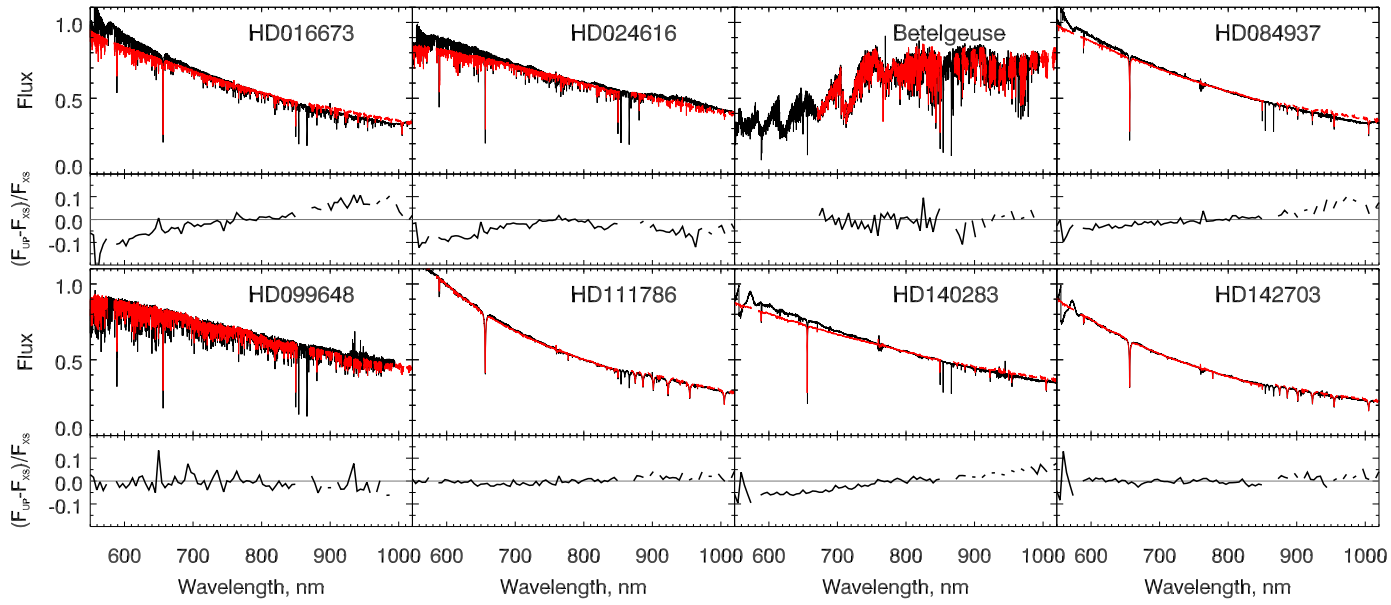

Figure 18. Spectra of eight stars from UVES-POP (red) and X-Shooter DR3 (black).

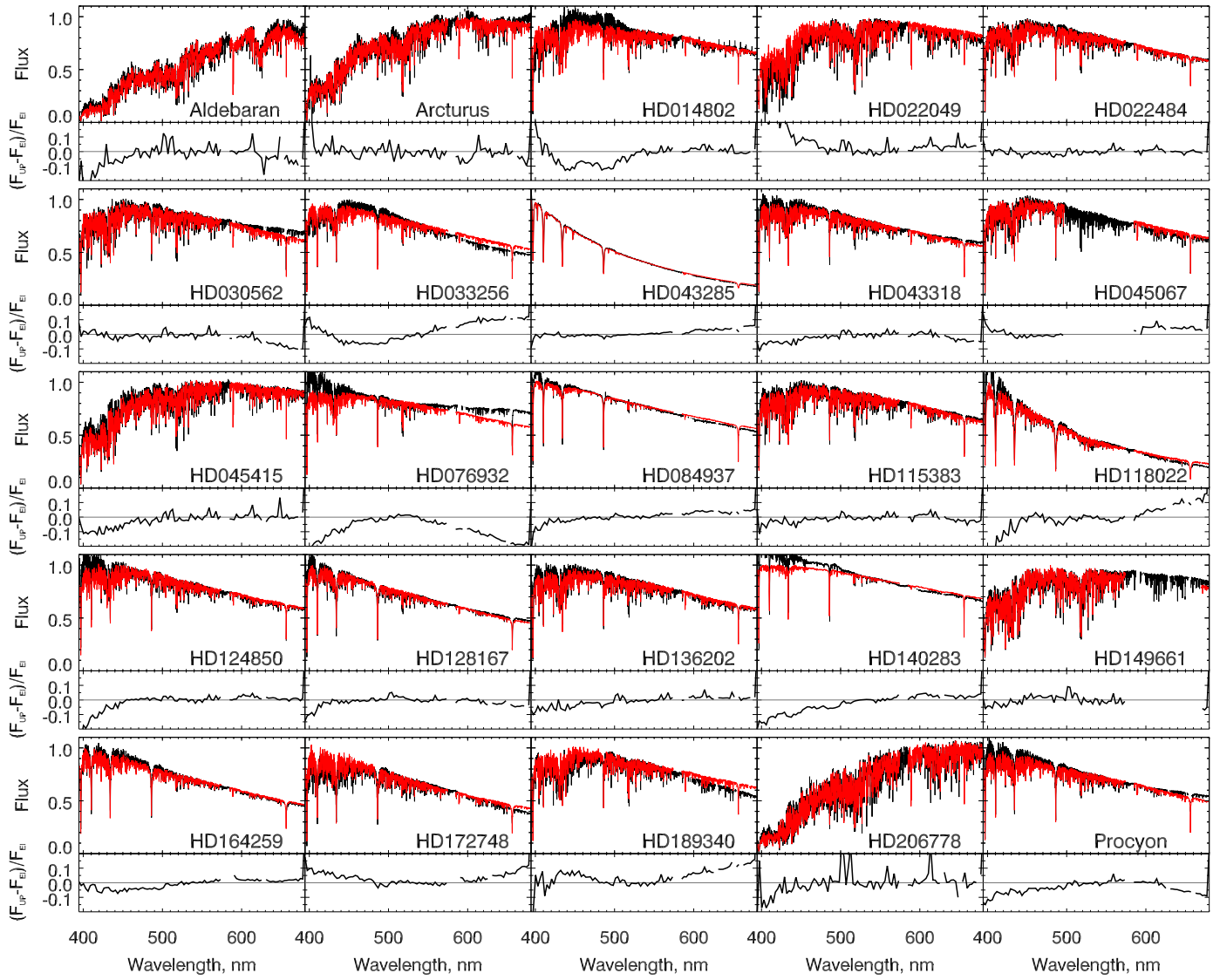

Figure 19. Spectra of 25 stars from UVES-POP (red) and ELODIE (black).

ORCID iDs

Sviatoslav B. Borisov https://orcid.org/0000-0002-2516-9000
Igor V. Chilingarian https://orcid.org/0000-0002-7924-3253
Evgenii V. Rubtsov https://orcid.org/0000-0001-8427-0240
Cédric Ledoux https://orcid.org/0000-0002-7864-3327
Claudio Melo https://orcid.org/0000-0002-6090-8446
Kirill A. Grishin https://orcid.org/0000-0003-3255-7340
Ivan Yu. Katkov https://orcid.org/0000-0002-6425-6879
Vladimir S. Goradzhanov https://orcid.org/0000-0002-2550-2520
Anton V. Afanasiev https://orcid.org/0000-0002-8220-0756
Anastasia V. Kasparova https://orcid.org/0000-0002-1091-5146
Anna S. Saburova https://orcid.org/0000-0002-4342-9312

References

Afanasiev, A. V., Chilingarian, I. V., Mieske, S., et al. 2018, MNRAS, 477, 4856
Allard, F., Homeier, D., & Freytag, B. 2012, RSPTA, 370, 2765
Arentsen, A., Prugniel, P., Gonneau, A., et al. 2019, A&A, 627, A138
Bagnulo, S., Jehin, E., Ledoux, C., et al. 2003, Msngr, 114, 10
Ballester, P., Modigliani, A., Boitquin, O., et al. 2000, Msngr, 101, 31
Barber, C. B., Dobkin, D. P., & Huhdanpaa, H. 1996, ACM Trans. Math. Softw., 22, 469
Barrado y Navascués, D., Stauffer, J. R., Jayawardhana, R., et al. 2004, ApJ, 614, 386
Bessell, M. S. 2000, PASP, 112, 961
Bessell, M. S. 2005, ARA&A, 43, 293
Borisov, S., Prantzos, N., & Charbonnel, C. 2022, A&A, 668, A181
Bowers, C. W., & Lindler, D. 2003, HST Calibration Workshop: Hubble after the Installation of the ACS and the NICMOS Cooling System, ed. S. Arribas, A. Koekemoer, & B. Whitmore, (Baltimore, MD: Space Telescope Science Institute), 127
Boyle, R. P., Vrba, F. J., Smriglio, F., Dasgupta, A. K., & Straizys, V. 1996, BaltA, 5, 231
Bruzual, G., & Charlot, S. 2003, MNRAS, 344, 1000
Buder, S., Sharma, S., Kos, J., et al. 2021, MNRAS, 506, 150
Cappellari, M., & Emsellem, E. 2004, PASP, 116, 138
Chen, Y.-P., Trager, S. C., Peletier, R. F., et al. 2014, A&A, 565, A117
Chilingarian, I. V., Cayatte, V., & Bergond, G. 2008, MNRAS, 390, 906
Chilingarian, I. V., Mieske, S., Hilker, M., & Infante, L. 2011, MNRAS, 412, 1627
Cousins, A. W. J. 1976, MmRAS, 81, 25
Creevey, O. L., Sordo, R., Pailler, F., et al. 2022, arXiv:2206.05864
Dalton, G. B., Caldwell, M., Ward, A. K., et al. 2006, Proc. SPIE, 6269, 62690X

De Pascale, M., Worley, C. C., de Laverny, P., et al. 2014, A&A, 570, A68
Dekker, H., D'Odorico, S., Kaufer, A., Delabre, B., & Kotzlowski, H. 2000, Proc. SPIE, 4008, 534
ESO CPL Development Team 2015, EsoRex: ESO Recipe Execution Tool, Astrophysics Source Code Library, ascl:1504.003
Evans, D. W., Riello, M., De Angeli, F., et al. 2018, A&A, 616, A4
Fitzpatrick, E. L. 1999, PASP, 111, 63
Francis, K. J., Drinkwater, M. J., Chilingarian, I. V., Bolt, A. M., & Firth, P. 2012, MNRAS, 425, 325
Fukugita, M., Ichikawa, T., Gunn, J. E., et al. 1996, AJ, 111, 1748
Gaia Collaboration, Babusiaux, C., van Leeuwen, F., et al. 2018, A&A, 616, A10
Gaia Collaboration, Prusti, T., de Bruijne, J. H. J., et al. 2016, A&A, 595, A1
Gaia Collaboration, Vallenari, A., Brown, A. G. A., et al. 2022, arXiv:2208.00211
Gonneau, A., Lyubenova, M., Lançon, A., et al. 2020, A&A, 634, A133
González Delgado, R. M., Cerviño, M., Martins, L. P., Leitherer, C., & Hauschildt, P. H. 2005, MNRAS, 357, 945
González-Fernández, C., Hodgkin, S. T., Irwin, M. J., et al. 2018, MNRAS, 474, 5459
Green, G. M. 2018, JOSS, 3, 695
Green, G. M., Schlafly, E. F., Finkbeiner, D., et al. 2018, MNRAS, 478, 651
Green, G. M., Schlafly, E. F., Finkbeiner, D. P., et al. 2015, ApJ, 810, 25
Gregg, M. D., Silva, D., Rayner, J., et al. 2006, The 2005 HST Calibration Workshop: Hubble After the Transition to Two-Gyro Mode, ed. A. M. Koekemoer, P. Goudfrooij, & L. L. Dressel, (Greenbelt, MD: Goddard Space Flight Center), 209
Guiderdoni, B., & Rocca-Volmerange, B. 1987, A&A, 186, 1
Hanuschik, R. W. 2003, A&A, 407, 1157
Henden, A. A., Levine, S., Terrell, D., et al. 2018, AAS Meeting, 232, 223.06
Hernandez, S., Larsen, S., Trager, S., Kaper, L., & Groot, P. 2018, MNRAS, 476, 5189
Hobbs, L. M. 1974, ApJ, 191, 381
Høg, E., Fabricius, C., Makarov, V. V., et al. 2000, A&A, 355, L27
Husser, T. O., Wende-von Berg, S., Dreizler, S., et al. 2013, A&A, 553, A6
Johnson, H. L., & Mitchell, R. I. 1975, RMxAA, 1, 299
Jones, A., Noll, S., Kausch, W., Szyszka, C., & Kimeswenger, S. 2013, A&A, 560, A91
Jordi, C., Gebran, M., Carrasco, J. M., et al. 2010, A&A, 523, A48
Kornilov, V., Mironov, A., & Zakharov, A. 1996, BaltA, 5, 379
Lançon, A., & Wood, P. R. 2000, A&AS, 146, 217
Le Borgne, J.-F., Bruzual, G., Pelló, R., et al. 2003, A&A, 402, 433
Lebreton, Y., & Reese, D. R. 2020, A&A, 642, A88
Markwardt, C. B. 2009, in ASP Conf. Ser. 411, Astronomical Data Analysis Software and Systems XVIII, ed. D. A. Bohlender, D. Durand, & P. Dowler (San Francisco, CA: ASP), 251
Mishenina, T. V., Soubiran, C., Kovtyukh, V. V., & Korotin, S. A. 2004, A&A, 418, 551
Montegriffo, P., De Angeli, F., Andrae, R., et al. 2022, arXiv:2206.06205
Noll, S., Kausch, W., Barden, M., et al. 2012, A&A, 543, A92
Oke, J. B., & Gunn, J. E. 1983, ApJ, 266, 713
Poznanski, D., Prochaska, J. X., & Bloom, J. S. 2012, MNRAS, 426, 1465
Prugniel, P., & Soubiran, C. 2001, A&A, 369, 1048
Prugniel, P., & Soubiran, C. 2004, arXiv:astro-ph/0409214
Prugniel, P., Soubiran, C., Koleva, M., & Le Borgne, D. 2007, arXiv:astro-ph/0703658
Rayner, J. T., Cushing, M. C., & Vacca, W. D. 2009, ApJS, 185, 289
Recio-Blanco, A., de Laverny, P., Palicio, P. A., et al. 2022, arXiv:2206.05541
Rejkuba, M., Dubath, P., Minniti, D., & Meylan, G. 2007, A&A, 469, 147
Rosen, J., & Marcia, R. 2004, Comput. Optim. Appl., 28, 173
Rubtsov, E., Chilingarian, I., Katkov, I., et al. 2021, arXiv:2112.03413
Samus', N. N., Kazarovets, E. V., Durlevich, O. V., Kireeva, N. N., & Pastukhova, E. N. 2017, ARep, 61, 80
Sánchez-Blázquez, P., Peletier, R. F., Jiménez-Vicente, J., et al. 2006, MNRAS, 371, 703
Skrutskie, M. F., Cutri, R. M., Stiening, R., et al. 2006, AJ, 131, 1163
Soubiran, C., Le Campion, J.-F., Brouillet, N., & Chemin, L. 2016, A&A, 591, A118
Taylor, M. A., Puzia, T. H., Harris, G. L., et al. 2010, ApJ, 712, 1191
Valdes, F., Gupta, R., Rose, J. A., Singh, H. P., & Bell, D. J. 2004, ApJS, 152, 251
Vazdekis, A., Sánchez-Blázquez, P., Falcón-Barroso, J., et al. 2010, MNRAS, 404, 1639
Verro, K., Trager, S. C., Peletier, R. F., et al. 2022, A&A, 660, A34
Villanova, S., Carraro, G., & Saviane, I. 2009, A&A, 504, 845
Villaume, A., Conroy, C., Johnson, B., et al. 2017, ApJS, 230, 23
Voggel, K. T., Seth, A. C., Neumayer, N., et al. 2018, ApJ, 858, 20
Wenger, M., Ochsenbein, F., Egret, D., et al. 2000, A&AS, 143, 9
Worley, C. C., de Laverny, P., Recio-Blanco, A., Hill, V., & Bijaoui, A. 2016, A&A, 591, A81
Yan, R., Chen, Y., Lazarz, D., et al. 2019, ApJ, 883, 175
Yee, S. W., Petigura, E. A., & von Braun, K. 2017, ApJ, 836, 77